

SPINELS FOR USE AS METHANE REFORMING CATALYSTS IN
FUEL FLEXIBLE SOLID OXIDE FUEL CELLS

BY

KATELYN CRYSTAL GLASS

A THESIS
SUBMITTED TO THE FACULTY OF

ALFRED UNIVERSITY

IN PARTIAL FULFILLMENT OF THE REQUIREMENTS
FOR THE DEGREE OF

MASTER OF SCIENCE

IN

CERAMIC ENGINEERING

ALFRED, NEW YORK
NOVEMBER 2014

Alfred University theses are copyright protected and may be used for education or personal research only. Reproduction or distribution in part or whole is prohibited without written permission from the author.

Signature page may be viewed at Scholes Library, New York State College of Ceramics, Alfred University, Alfred, New York.

SPINELS FOR USE AS METHANE REFORMING CATALYSTS IN
FUEL FLEXIBLE SOLID OXIDE FUEL CELLS

BY

KATELYN GLASS

B.S. ALFRED UNIVERSITY (2009)

SIGNATURE OF AUTHOR _____

APPROVED BY _____

DR. SCOTT T. MISTURE, ADVISOR

DR. WILLIAM CARTY, ADVISORY COMMITTEE

DR. YIQUAN WU, ADVISORY COMMITTEE

CHAIR, ORAL THESIS DEFENSE

ACCEPTED BY _____

DR. DOREEN D. EDWARDS, DEAN
KAZUO INAMORI SCHOOL OF ENGINEERING

ACKNOWLEDGMENTS

Thank you to my parents for putting up with me and supporting me throughout my school years. Thank you to all of the friends I met in Alfred, I love and miss all of you. Thank you to all of my professors and advisors who taught me so much. Thank you to my baby girl Jade, for being the best dog ever. Mama loves you.

TABLE OF CONTENTS

	Page
Acknowledgments	iii
Table of Contents	iv
List of Tables	vi
List of Figures	vii
Abstract	iii
I. INTRODUCTION.....	1
A. Spinels For Methane Steam Reforming.....	2
B. Ceramic SOFC Anode Materials.....	3
C. Use of Hydrocarbon Fuels with SOFCs	4
D. Regeneration.....	5
E. Thesis Scope.....	6
II. NI- AND CO- CONTAINING ALUMINATE SPINEL CATALYSTS FOR STEAM REFORMING	7
A. Introduction	7
B. Experimental Procedure.....	8
1. Powder Synthesis.....	8
a. Solid State Synthesis.....	8
b. Heat Treatment.....	8
c. Open System Reduction.....	9
2. Characterization.....	9
a. TGA/DTA.....	9
b. Room Temperature X-ray Diffraction	10
c. High Temperature X-ray Diffraction in Flowing 4% H ₂ /N ₂	10
d. Standard Voltage Scanning Electron Microscopy	11
e. Catalysis Measurement.....	11
C. Results and discussion	12
1. Powder Properties.....	12
2. Reduction Kinetics (TGA/HTXRD).....	25
3. Oxidation/Reduction Cycling	31
4. Catalysis Studies.....	35
5. Exposure to Methane	40
D. Summary and Conclusions	44

E. Future Work.....	44
III. EFFECT OF SPINEL ADDITIONS ON NI/YSZ CELL PERFORMANCE IN HYDROCARBON FUELS.....	46
A. Experimental Procedure.....	46
1. Cell Preparation	46
2. Fuel Cell Testing Setup.....	46
3. Characterization	47
a. Power Density Measurements.....	47
b. Standard Voltage Scanned Electron Microscopy.....	47
B. Results and Discussion	47
1. Cell Performance	47
a. Cell Structure	47
b. Effect of Spinel Additions.....	48
C. Future Work.....	51
D. Summary and Conclusions	51
REFERENCES.....	52

LIST OF TABLES

	Page
Table 1. Dwell Parameters for Calcination Heat Treatment Profiles	8
Table 2. Coefficients of Thermal Expansion of Defect Spinels and Metals from HTXRD pattern refinement.	28

LIST OF FIGURES

	Page
Figure 1. Schematic of solid oxide fuel cell highlighting reactions occurring in each component.....	2
Figure 2. Comparison of the XRD data for three compositions calcined at 1500°C for 8 hours and reduced at 800°C for 8 hours.	12
Figure 3. Spinel peak in NiAl ₂ O ₄ calcined at 1300-1600°C and reduced at 900°C.	13
Figure 4. Spinel peak in Ni _{0.5} Co _{0.5} Al ₂ O ₄ calcined at 1300-1600°C and reduced at 900°C.	13
Figure 5. Spinel peak in CoAl ₂ O ₄ calcined at 1300-1600°C and reduced at 900°C.	14
Figure 6. Metal peak in NiAl ₂ O ₄ calcined at 1300-1600°C and reduced at 900°C.	14
Figure 7. Metal peak in NiAl ₂ O ₄ calcined at 1300-1600°C and reduced at 900°C.	15
Figure 8. Change in degree of faceting in NiAl ₂ O ₄ can be seen as calcination temperature increases.	16
Figure 9. Change in degree of faceting in Ni _{0.5} Co _{0.5} Al ₂ O ₄ can be seen as calcination temperature increases.	17
Figure 10. Change in degree of faceting in CoAl ₂ O ₄ can be seen as calcination temperature increases.	18
Figure 11. SEM showing increase in size of Ni metal particles with increasing reduction temperature for NiAl ₂ O ₄ powders calcined at 1300°C for 36 hours.	19
Figure 12. Increase in size of Ni metal particles with increase in reduction temperature on NiAl ₂ O ₄ calcined at 1400°C for 8 hours.	19
Figure 13. NiAl ₂ O ₄ calcined at 1500°C for 8 hours and reduced at 700, 800, and 900°C for 8 hours.	20
Figure 14. NiAl ₂ O ₄ calcined at 1600°C for 8 hours and reduced for 8 hours at 700, 800, and 900°C.	20

Figure 15. $\text{Ni}_{0.5}\text{Co}_{0.5}\text{Al}_2\text{O}_4$ calcined at 1300°C for 36 hours and reduced for 8 hours at 700, 800, and 900°C.	21
Figure 16. $\text{Ni}_{0.5}\text{Co}_{0.5}\text{Al}_2\text{O}_4$ calcined at 1400°C for 8 hours and reduced for 8 hours at 700, 800, and 900°C	21
Figure 17. $\text{Ni}_{0.5}\text{Co}_{0.5}\text{Al}_2\text{O}_4$ calcined at 1500°C for 8 hours and reduced for 8 hours at 700, 800, and 900°C	22
Figure 18. $\text{Ni}_{0.5}\text{Co}_{0.5}\text{Al}_2\text{O}_4$ calcined at 1600°C for 8 hours and reduced for 8 hours at 700, 800, and 900°C	22
Figure 19. CoAl_2O_4 calcined at 1300°C for 36 hours and reduced for 8 hours at 700, 800, and 900°C.	23
Figure 20. CoAl_2O_4 calcined at 1400°C for 8 hours and reduced for 8 hours at 700, 800, and 900°C.	23
Figure 21. CoAl_2O_4 calcined at 1500°C for 8 hours and reduced for 8 hours at 700, 800, and 900°C.	24
Figure 22. CoAl_2O_4 calcined at 1600°C for 8 hours and reduced for 8 hours at 700, 800, and 900°C.	24
Figure 23. Ni- and Co- Al_2O_4 spinels calcined at 1500°C for 8 hours and reduced in 4% H_2 /96% N_2 for 48 hours.....	25
Figure 24. Lattice parameter of the defect spinel support for $\text{Ni}_x\text{Co}_{(1-x)}\text{Al}_2\text{O}_4$ with decrease in temperature.....	27
Figure 25. Lattice parameter of metallic nanoparticles for $\text{Ni}_x\text{Co}_{(1-x)}\text{Al}_2\text{O}_4$ with decrease in temperature.	27
Figure 26. Metal peak shift between the three Ni- and Co- containing spinel samples, each calcined for 8 hours at 1600°C and reduced at 900°C for 8 hours in flowing hydrogen.	29
Figure 27. TGA analysis of aluminate and ferrite spinels.	30
Figure 28. TGA data with calculated reduction limits.....	31
Figure 29. HTXRD patterns for the reduction of $\text{Ni}_{0.5}\text{Co}_{0.5}\text{Al}_2\text{O}_4$ to 1200°C.	32

Figure 30. HTXRD patterns for reoxidation of $\text{Ni}_{0.5}\text{Co}_{0.5}\text{Al}_2\text{O}_4$ to 1200°C	32
Figure 31. HTXRD patterns showing reduction and reoxidation of CoAl_2O_4	33
Figure 32. XRD patterns of $\text{Ni}_{0.5}\text{Co}_{0.5}\text{Al}_2\text{O}_4$ spinel over 3 cycles, showing no degradation in phase composition over the 3 cycles.....	34
Figure 33. SEM images showing initial reduction with significant coarsening, reoxidation, and re-reduction of NiAl_2O_4 and CoAl_2O_4 samples.	34
Figure 34. Methane reforming performance on $\text{Ni}_{0.5}\text{Mg}_{0.5}\text{Al}_2\text{O}_4$ catalyst under the conditions of 850°C , 32.5% CH_4 , 64.5% CO_2 , 3.0% N_2 and GHSV = 60,000 hr^{-1}	35
Figure 35. Methane reforming performance on NiAl_2O_4 catalyst under the conditions of 850°C , 32.5% CH_4 , 64.5% CO_2 , 3.0% N_2 and GHSV = 60,000 hr^{-1}	36
Figure 36. Methane reforming performance on $\text{Ni}_{0.5}\text{Co}_{0.5}\text{Al}_2\text{O}_4$ catalyst under the conditions of 850°C , 32.5% CH_4 , 64.5% CO_2 , 3.0% N_2 and GHSV = 60,000 hr^{-1}	36
Figure 37. Methane reforming performance on NiAl_2O_4 (LT) catalyst under the conditions of $650\text{-}850^\circ\text{C}$, 32.5% CH_4 , 64.5% CO_2 , 3.0% N_2 and GHSV = 60,000 hr^{-1}	37
Figure 38. Methane reforming performance on NiAl_2O_4 catalyst under the conditions of $650\text{-}850^\circ\text{C}$, 32.5% CH_4 , 64.5% CO_2 , 3.0% N_2 and GHSV = 60,000 hr^{-1}	37
Figure 39. Effect of H_2S on methane reforming performance over NiAl_2O_4 (LT) catalyst under the conditions of 850°C , 20 ppm H_2S , 29.3% CH_4 , 58.1% CO_2 , 12.6% N_2 and GHSV = 60,000 hr^{-1}	38
Figure 40. Effect of H_2S on methane reforming performance over NiAl_2O_4 catalyst under the conditions of 850°C , 20 ppm H_2S , 29.3% CH_4 , 58.1% CO_2 , 12.6% N_2 and GHSV = 60,000 hr^{-1}	38
Figure 41. Post-situ SEM images of NiAl_2O_4 samples sent for catalytic activity testing. The image on the left shows a less faceted defect spinel calcined at 1300°C 36hrs. and the image on the right shows a more faceted defect spinel calcined at 1500°C 8hrs.	40

Figure 42. CoAl_2O_4 calcined at 1300°C for 36 hours and reduced in methane at 850°C for 8 hours. Metallic Co particle can be seen atop a carbon filament in the upper left.	41
Figure 43. CoAl_2O_4 calcined at 1400°C for 8 hours, reduced in flowing H_2 at 900°C for 8 hours, and exposed to methane at 800°C for 3 hours. Variations in size of the carbon filaments can be seen, which are caused by variations in size of metal particles.	42
Figure 44. $\text{Ni}_{0.5}\text{Co}_{0.5}\text{Al}_2\text{O}_4$ calcined at 1500°C for 8 hours, reduced in CH_4 for 8 hours, then exposed to air at 350°C to remove carbon without reoxidizing.....	43
Figure 45. NiAl_2O_4 calcined at 1300°C for 36 hours and reduced in CH_4 for 8 hours, then exposed to air at 350°C to remove carbon buildup. Very short carbon filaments can be seen (highlighted) with small Ni metal particles on top of them.....	44
Figure 46. Schematic showing Probostat within furnace and a cross-section showing the cell placement inside the outer alumina tube.....	47
Figure 47. SEM image of cross-section of YSZ electrolyte coated with $\text{NiAl}_2\text{O}_4/\text{NiO}/\text{YSZ}$ composite anode.	48
Figure 48. Power density using hydrogen fuel of cells containing 3 different spinels in the anode vs. a traditional NiO/YSZ anode.	49
Figure 49. Power density using methane fuel of 3 different spinel compositions included in the anode, shown vs. a traditional NiO/YSZ anode.....	50
Figure 50. Voltage curves for samples containing 3 different spinel compositions vs. traditional NiO/YSZ anode.	51

ABSTRACT

Several compositions of Ni- and Co- containing aluminate spinels have been synthesized in a reproducible manner, each of which are potential catalyst materials for methane reforming in-situ during SOFC operation. Reduction and reoxidation cycles can be performed at or below typical intermediate temperature SOFC operating temperatures. The defect spinel structure remains intact if a zirconia stabilizer is used. The microstructure of the defect spinel support following reduction varies depending on calcination temperature. The faceted microstructure of the defect spinel support and the metallic particles contributes to the excellent catalytic activity of the material. NiAl_2O_4 and $\text{Ni}_{0.5}\text{Co}_{0.5}\text{Al}_2\text{O}_4$ catalysts had nearly 100% CH_4 conversion over 16 hours at $\text{GHSV}=60,000\text{hr}^{-1}$, with the Co-containing sample losing some activity over the test period. H_2 and CO selectivities remained around 80% throughout the test. Less faceted defect spinel catalyst conversion percentages increased with reactor temperature, indicating further reduction of metal from the defect spinel support during testing. Using methane fuel containing 20ppm H_2S , conversion and CO selectivity dropped to 0% after 6 and 12 hours in less faceted and more faceted defect spinels, respectively. The spinels can be reduced in methane but acquire a significant amount of carbon buildup with low concentrations of CO. The spinels have been incorporated into a Ni/YSZ cermet anode in 10 and 20 weight percent quantities to study the effect of the spinels on the cell performance and microstructure. Peak power densities in H_2 fuel were 0.0153, 0.0076, 0.0025, and 0.0153 W/cm^2 for samples containing NiAl_2O_4 , $\text{Ni}_{0.5}\text{Co}_{0.5}\text{Al}_2\text{O}_4$, CoAl_2O_4 , and no spinel, respectively. In CH_4 fuel, peak power densities were 0.0115, 0.0089, 0.0089, and 0.0127 W/cm^2 for samples containing NiAl_2O_4 , $\text{Ni}_{0.5}\text{Co}_{0.5}\text{Al}_2\text{O}_4$, CoAl_2O_4 , and no spinel, respectively. Increasing Co content reduces peak power density values, with the NiAl_2O_4 -containing sample having a similar peak power density to the control Ni/YSZ sample.

I. INTRODUCTION

Due to increased environmental concerns, the energy industry is focusing on use of renewable fuel sources as an alternative to fossil fuels. Similar concerns have also driven the development of solid oxide fuel cell (SOFC) technology as SOFCs are fuel flexible and can be made in a wide range of sizes. The high operation temperatures needed to activate the electrolyte also allow internal reforming of hydrocarbon fuels. The operation of a SOFC is detailed in Figure 1, with equations explaining reactions occurring at the anode in an internally reforming fuel cell. Several obstacles need to be overcome before use of “dirty” biofuels with SOFCs becomes feasible. First, coking of the Ni metal anode catalyst due to hydrocarbon content in the fuel can deactivate the catalyst. Hydrogen sulfide present in the fuel stream can also poison the catalyst and degrade its effectiveness. Lastly, cathodes can be deactivated by the Cr found in stainless steel interconnects. A proposed solution is the use of oxide-based anodes that can refresh themselves after use through oxidation-reduction cycles. The oxide is reduced in the fuel stream to form catalytic metal nanoparticles supported by a defect spinel. Reabsorbing the spent catalyst into the oxide through oxidation then reducing the oxide to form metal nanoparticles again reactivates the anode. This solution is particularly attractive since spinels are versatile and a wide range of compositions is possible. The temperatures reached by intermediate temperature SOFCs (ITSOFCs) are adequate for carrying out the reoxidation process, which starts at approximately 750°C.¹

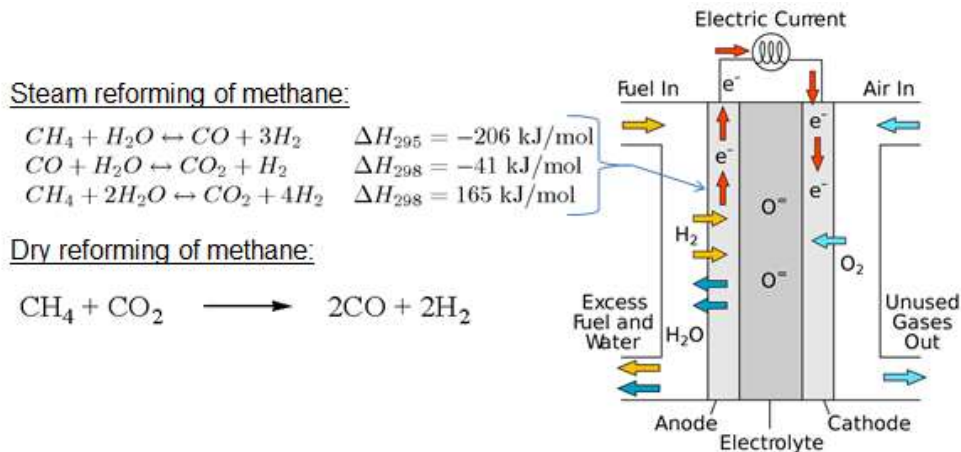


Figure 1. Schematic of solid oxide fuel cell highlighting reactions occurring in each component.¹¹²

A. Spinel For Methane Steam Reforming

Numerous studies have focused on steam reforming of methane and other hydrocarbons for various applications. The high operating temperatures of solid oxide fuel cells allows internal steam reforming of hydrocarbons to produce H_2 fuel, unlike other types of fuel cells. SOFCs that rely on internal reforming of hydrocarbon fuels face issues similar to those that have plagued commercial catalytic steam reforming processes for some time.^{2,3} The catalysts used in these processes are typically Ni with a $\gamma\text{-Al}_2\text{O}_3$ or spinel support.⁴⁻⁶ The sintering behavior of the metallic particles and the stability of the support following in-situ reduction have been studied.⁷⁻⁹ Impurities typically found in fuels, such as sulfur, poison the catalyst.¹⁰⁻¹⁴ In some cases, exposure to sulfur in fuel causes a phase transformation and failure due to structural degradation.^{15,16} Both problems have been encountered for some time in the field of commercial catalytic steam reforming.^{2,17} The mechanisms behind coking and sulfur poisoning in SOFC anodes have been recently reviewed.¹⁸ Sintering of the Ni metal particles on the surface of the ceramic support can also decrease surface area of the catalyst therefore decreasing catalytic activity.¹⁹

AB_2O_4 -type spinels form metallic A particles following reduction while B particles remain as part of the spinel phase. When Cu is found on the A site, the spinel becomes an oxide upon reduction when $\text{B}=\text{Mn}$ ²⁰, Cr ^{21,22}, or Al ²³. However, when $\text{B}=\text{Fe}$ or Ga ²³, the spinel structure remained after reduction. Similarly, when $\text{A}=\text{Ni}$, the spinel structure remains when $\text{B}=\text{Al}$ ²⁴ or Fe ²⁵. Tanaka's group introduced a possible solution to the issue of coking and poisoning of automotive catalysts through metal nanoparticle regeneration.^{26,27} An oxide material containing a

minimum of 2 cations was reduced to form metal nanoparticles and an oxide support. The nanoparticles undergo particle growth and poisoning as a result of high temperatures and sulfur, etc. during use. The material can be oxidized, thereby reabsorbing the metal nanoparticles into the oxide support. Afterwards, the oxide is reduced again to form clean, active nanoparticulate metal catalyst.

B. Ceramic SOFC Anode Materials

Recent review articles provide an overview of SOFC electrode material research.²⁸ It has been found that traditional Ni metal SOFC anodes can be partially or fully replaced by oxides.²⁹ Recent review articles provide an overview of SOFC anodes used in dirty hydrocarbon fuels.³⁰⁻³² A combination of Ni and electrolyte material, usually YSZ, is used commonly in SOFC anodes. Liu et al. showed that doping with Nb improved sulfur resistance.³³ Most recent research in SOFC anodes focuses on perovskite oxides, such as (La,Sr)VO₃³⁴⁻³⁶ (LSV) and (La,Sr)(Cr,Mn)O₃ (LSCM)^{37,38}, with high ionic and electronic conductivities.³⁹⁻⁴⁷ These mixed ionic and electronic conductors (MIECs) can be used alone or with added Ni or other catalytic metals. Doped perovskites have been found to be stable in H₂S containing fuel.⁴⁸ Performance of a LSCM/YSZ anode has been improved by adding nanoscale Gd_{0.2}Ce_{0.8}O_{1.9} which performs well in methane based fuels with decent sulfur tolerance.⁴⁹ Adding 3-10 atom % Ni to LaCrO₃-based perovskites on the Cr site improves catalytic activity by forming metallic Ni nanoparticles on the surface upon reduction.⁵⁰ Pyrochlore-type oxides such as Gd₂Ti_{2-x}Mo_xO₇ (x = 1.0 and 1.4) have been studied with Gd₂TiMoO₇ showing promise for H₂S removal and sulfur tolerance in composite with (Li_{0.62}, K_{0.38})₂CO₃ electrolyte.⁵¹ A Sm_{1-x}Ce_xFeO_{3-δ} perovskite anode showed an 0.690V OCV at 450°C and did not coke in dry methane, indicating promise as a low temperature SOFC anode.¹⁰⁵

Prior research focused on SrTiO₃ with added dopants to allow reduction in the fuel stream.⁵²⁻⁵⁴ These materials, including Sr_{1-x/2}Ti_{1-x}Nb_xO₃, have low ionic conductivity. Later materials include La₄Sr_{x-4}Ti_xO_{3x+2}, an oxygen-excess layered perovskite in conjunction with YSZ. This composite had promising results when used with methane fuel. Similarly, (La/Sr)_{1-x}Cr_{0.5-x}Mn_{0.5}O_{3-δ} showed promising results comparable to Ni/YSZ in hydrocarbon fuels.^{49,55-59} Mechanisms governing electrochemical performance of La_{0.4}Sr_{0.6}Ti_{1-x}Mn_xO_{3-δ} (LSTM) perovskites have been studied, however LSTM has poor catalytic activity when used with methane.⁶⁰ A La_{0.3}Sr_{0.7}TiO₃ (LST)-Ni/YSZ bi-layer anode used in dry H₂/CH₄/CO/CO₂ fuel mix

showed that conversion of CH_4 depends on anode polarization. CO forms at low current densities and H_2O and CO_2 form at higher current densities.⁶¹

Numerous transition metal substitutions and oxide/metal composites based on the chromate material have been studied.⁶²⁻⁶⁴ Barnett's group found that addition of Ni or Ru to the oxide leaves Ni or Ru nanoparticles on the oxide surface following reduction, which improves anode polarization under dry and wet H_2 . The Ru performs better as it does not coarsen over time like Ni. Similarly, Sr_2MMoO_6 ($\text{M} = \text{Co}, \text{Ni}$) performs better in wet CH_4 when $\text{M}=\text{Co}$ due to Co metal reducing from the oxide to form catalytic metal nanoparticles on the surface. Coking resistance of lanthanum molybdates used with wet methane was higher than for dry methane, indicating that steam additions may be beneficial.¹⁰⁶

Numerous ceria-based ceramic anode studies have been published recently. Co-doping CeO_2 based material with Y and Yb has shown potential as both an internal reforming anode as well as sulfur removal aid.¹⁰⁷ A Cu- CeO_2 layer on traditional Ni/YSZ anode has been shown to improve performance in CO-rich syngas by facilitating the water gas shift reaction.¹⁰⁸ $\text{CeO}_2\text{-Al}_2\text{O}_3$ operated at 800-900°C showed potential for use in direct ethanol fuel.¹⁰⁹ Ni- $\text{Ce}_{0.8}\text{Zr}_{0.2}\text{O}_2$ made using the glycine nitrate process showed significant catalytic activity due to small nickel metal particle size and strong interaction between the support and catalyst nanoparticles. Peak powder densities of 536 mW/cm^2 at 700°C were reached when EtOH/steam fuel was used on a SOFC with a Ni- $\text{Ce}_{0.8}\text{Zr}_{0.2}\text{O}_2$ functional anode layer.¹¹⁰

C. Use of Hydrocarbon Fuels with SOFCs

Recent review articles summarize the current state of knowledge regarding use of dirty hydrocarbons with SOFCs.^{30,31,48} Hill's group has done extensive research on the use of hydrocarbon fuels with SOFCs,⁶⁵ and has published a review on the use of liquid hydrocarbon fuels in portable SOFC applications.⁶⁶ Ni/YSZ, Ni/ceria, Cu/ceria and LSCM anode compositions were made to try to elucidate the effects of carbon on varying compositions. Carbon deposited is found to be influenced by the presence of an applied potential, the presence of ceria, the hydrogen content in the feed, and the oxygen content in the feed.⁶⁷ Similar studies have also been done to study the influence of sulfur contamination in hydrogen.⁶⁸ Ni/YSZ anodes that had suffered coking were found to obtain less damage during carbon removal when H was used rather than O during temperature programmed hydrogenation.⁶⁹ The carbon formed on Cu-Ni/YSZ

prepared using microwave irradiation in dry methane was found to be more reactive than that formed on conventional Ni/YSZ anodes.^{70,71} Cu-Co(Ru)/Zr_{0.35}Ce_{0.65}O₂ anodes used with methanol and ethanol were exposed to humidified hydrogen after coking to recover cell performance that, in some cases, exceeded the original values.⁷² The variations in cell performance in electrolyte-versus anode-supported cells with respect to carbon formation were also studied.⁶⁵

D. Regeneration

Regeneration of coked and sulfur poisoned nickel-based steam reforming catalysts has been done using CO₂ as an oxidant with steam. 80% of the original catalytic activity was present after regeneration with a decreased particle size.⁷³ A study of regenerative Co and Rh-based catalysts mixed with ZnO found that Co was more susceptible to coking and sulfur poisoning, but was easily reoxidized.⁷⁴ Ni/Mg(Al)O⁷⁵, Co⁷⁶, and Ni/Al₂O₃⁷⁷ catalysts containing trace Ru dopant regenerated during daily startup/shutdown procedures, with Ru assisting in regeneration. CuFe₂O₄ spinel catalysts have also been reformed during startup/shutdown.⁷⁸ Rh/CeO₂-ZrO₂ ethanol steam reforming catalysts acquire a carbon layer at 350°C which can be completely removed in oxygen at 212°C.^{79,80} Rh-Pt alloy ethanol steam reforming catalyst deposited on a ceramic monolith can be regenerated, however coking resistant degrades significantly after regeneration.⁸¹ Calcined commercial Mg-Al layered double hydroxides impregnated with Ni(II) and Pt(IV) nitrates can be used as catalysts for steam reforming of methane. The Mg_xAl_{1-x}O periclase acts as a Ni reservoir and assists regeneration through movement of Ni atoms between the surface and the inside of the crystal. Ni⁰ on the surface formed Ni²⁺ when exposed to steam and incorporated into Mg(Ni²⁺,Al)O periclase, while the Ni²⁺ ions in the periclase reduced to Ni⁰ by the hydrogen spillover to form small Ni⁰ particles on the catalyst surface.⁸² Pd-substituted (La,Sr)CrO₃-Æ with 50 wt% Ce_{0.9}Gd_{0.1}O_{2-δ} tested in La_{0.9}Sr_{0.1}Ga_{0.8}Mg_{0.2}O_{3-δ} electrolyte supported fuel cells at 800°C with humidified H₂ fuel showed regeneration behavior following degradation.¹¹⁰

Metal particle regeneration has recently been studied for use in automotive catalysts^{26,27,83,84} and in SOFCs^{85,86}. Reducible cations in oxide hosts reduce to form metallic nanoparticles supported by a remnant oxide. Following particle coarsening, coking, and sulfur poisoning, the catalyst is oxidized to resorb the metal into the oxide. The catalyst is then reduced out again to form fresh metal nanoparticles. Regenerative perovskite catalysts based on Rh, Pt, and Pd have been previously studied by Tanaka et al.⁸⁷⁻⁹⁰

E. Thesis Scope

The current state of knowledge suggests that MIEC oxides supporting dispersed metal nanoparticles are effective anodes in SOFC applications. The present work will focus on developing a highly effective oxide supported metal nanoparticle catalyst with the ability to refresh itself after damage caused by “dirty” biofuel streams. The anode structure will have 10-50 volume percent $(\text{TM}_{1-x}\text{A}_x)\text{B}_2\text{O}_4$ spinel where TM is a transition metal, A is Mg or another transition metal, and B is another metal such as Al, Ga, or Fe, among others. One transition metal needs to reduce in the fuel stream to form metal nanoparticles dispersed on the defect spinel support. The anode will have a balance of MIEC oxides and ion conducting oxides.

During the investigation, the role of each component in the reaction between the fuel stream and the anode will be thoroughly investigated to indicate optimal component materials. Quantitative data on the catalytic activity of the anodes made with varying component materials will be gathered in order to achieve this goal. The data will be combined to find an optimal percentage of spinel support, oxide ion conductor, and oxide MIEC in the anode.

Since spinels are able to incorporate both mono- and trivalent reducible A-site cations, several catalytic metals including Ni, Co, Cu, Mn, Ru, Pt, Pd, and Rh will be considered. B-site cations such as Cu, Fe, Rh, Mg, and Cr will be considered and their interaction with the catalyst will be investigated.

Some oxide supports may also supplement the catalytic activity of the anode, as seen with $\gamma\text{-Al}_2\text{O}_3$. Recent work has shown that $(\text{Ni,Mg})\text{Al}_2\text{O}_4$ forms a large number of oxygen vacancies leading to some amount of free volume in the material. Since this free volume will provide more active sites for catalysis, it may be useful in increasing anode efficiency.¹⁰⁶ The adsorption behavior of methane and hydrogen gases on these supports will be studied.

II. NI- AND CO- CONTAINING ALUMINATE SPINEL CATALYSTS FOR STEAM REFORMING

A. Introduction

NiAl_2O_4 spinel catalyst has shown 100% conversion of biodiesel to CO , CO_2 , H_2 , and CH_4 with little deactivation and no carbon deposit on the surface.⁹¹ NiAl_2O_4 reduces at 750°C in $7\%\text{H}_2/\text{Ar}$ and at 650°C in $7.5\%\text{CH}_4$ in N_2 , as evidenced by the methane dissociation starting at that temperature. Methane dissociation starts at a lower temperature, between $270\text{--}370^\circ\text{C}$ in samples reduced with hydrogen prior to being exposed to methane.⁹² Adding NiO excess to the spinel causes an increase in carbon formation due to increased size and decreased dispersion of Ni metal particles.⁹³ Use of 250% excess steam has been shown to inhibit coking, and thus prevent deactivation due to coking,⁹⁴

Many factors influence the behavior of the spinel with respect to methane decomposition. Studies of Ni for steam reforming indicate that adding a second metal may be beneficial.⁹⁵ Cobalt, another inexpensive catalytic metal, has also been studied for methane reforming.⁹⁶ A mixed oxide catalyst containing both Ni and Co was used for ethanol steam reforming. The selectivity to hydrogen increases with Co content at 820K , with the most selective formulation being the Ni -free mixed oxide.⁹⁷ A bimetallic 50:50 ratio of Ni to Co supported on ZrO_2 showed the highest catalytic activity for steam reforming of methane, as opposed to higher Co ratios.⁹⁸ Some studies indicate that the size of the catalytic metal particles plays a role in the selectivity of the catalyst.⁶

The best aspect of spinel as a catalyst is its' ability to regenerate by oxidation with exposure to air.⁷⁵ The volumetric changes associated with reoxidation may be severe enough to cause cracking in the anode, especially if high PO_2 is reached. The temperature at which both oxidation and reduction occurs is of interest, as is the temperature at which carbon deposits are removed.

The reduction of a transition metal from a spinel is a complex process, with many factors that must be monitored simultaneously, including the phases that are present, the weight percent of each, the grain size of each phase, and microstructural development. The microstructural features of concern include the fraction of the transition metal that forms on the surface versus in the bulk, particle shapes, and any cracking of the spinel matrix. This study investigates the reduction and reoxidation kinetics of the NiAl_2O_4 , $\text{Ni}_{0.5}\text{Co}_{0.5}\text{Al}_2\text{O}_4$, and CoAl_2O_4 spinels, their

catalytic performance as a function of catalytic metal particle size, and the effect of coking on their microstructures. The amount of weight gained as a result of reduction in methane and exposure to methane is of interest, as well as the movement of metal particles during removal of carbon filaments. Two ferrite spinel compositions were also synthesized and tested initially.

B. Experimental Procedure

1. Powder Synthesis

a. Solid State Synthesis

Solid state synthesis was used to produce the $\text{Ni}_x\text{Co}_{1-x}\text{Al}_2\text{O}_4$ ($x=1, 0.5,$ and 0), and $\text{Ni}_x\text{Cu}_{1-x}\text{Fe}_2\text{O}_4$ ($x=1, 0.5,$ and 0) each with 2.5 weight percent ZrO_2 to act as a stabilizer. NiO (97%, Fisher Scientific), Co_3O_4 (99.7%, Alfa Aesar), anhydrous Al_2O_3 (99%, Fisher Scientific), Cu_2O (99.95%, Alfa Products), Fe_2O_3 (99%, Fisher Scientific), and $\text{ZrO}(\text{NO}_3)_2 \cdot 6\text{H}_2\text{O}$ (99%, Acros Organics) were used as reactants. Thermogravimetric analysis was performed on the reactants to determine the amount of water lost on ignition, which was accounted for in calculating reactant quantities. Each batch was vibratory milled for 30 minutes in deionized water with alumina media in plastic jars. Zirconyl nitrate was dissolved completely in deionized water before being added. After milling, the slurry was dried on a hot plate and mixed in an alumina mortar and pestle.

b. Heat Treatment

Powders were calcined in an electric furnace using a heating rate of $5^\circ\text{C}/\text{min}$. Calcination temperatures and times can be found in Table 1. X-ray diffraction analysis was performed on each batch to ensure that single-phase spinel with a small amount of both monoclinic and tetragonal ZrO_2 .

Table 1. Dwell Parameters for Calcination Heat Treatment Profiles

Dwell Temperature ($^\circ\text{C}$)	Dwell Time (hours)
1100	120
1200	120
1300	36
1400	8
1500	8
1600	8

c. Open System Reduction

Reduction was carried out in an alumina tube furnace. A mass of 3g of each composition was placed in the furnace per run, in short alumina crucibles (CoorsTek) on an alumina setter plate. The placement of the samples in the furnace was approximately centered, verified using a measuring stick. The furnace was then closed and vacuum pumped to <0.1 Torr. The heating profile was started after achieving vacuum, with a rate of $5^{\circ}\text{C}/\text{min}$ to the target reduction temperature. The furnace temperature was regulated by an S-type thermocouple. Flowing hydrogen gas was introduced after shutting the vacuum tube valve and shutting off the vacuum pump. Once the dual capacitance manometer reached atmospheric pressure, the outlet valve was opened, allowing the flowing H_2 to pass through a bubbler before being released through a window. Flow was set to $10\text{ mL}/\text{min}$ for the duration of the experiment after the outlet valve was opened. The furnace was allowed to cool at $5^{\circ}\text{C}/\text{min}$ at the end of the dwell, with hydrogen flowing until $<100^{\circ}\text{C}$, at which temperature the flow was shut off. The evacuation and flow procedure was the same when using pure methane as a process gas. The furnace was opened and samples removed after temperature reached $<100^{\circ}\text{C}$. In cases where significant reduction occurred, powders were slightly consolidated and were broken up with a metal spatula.

2. Characterization

a. TGA/DTA

Both isothermal and non-isothermal TGA/DTA studies were carried out using a Setaram SETSYS Evolution, which has a $0.002\ \mu\text{g}$ resolution and $0.03\ \mu\text{g}$ noise RMS. The instrument uses background subtraction to increase accuracy. This is done by performing a measurement with empty crucibles under the exact conditions that will be used for a sample. The mass and DTA signals from this measurement are subtracted from subsequent measurements to remove experimental artifacts.

Optional equipment was used during reduction experiments to avoid damaging the platinum components with hydrogen. A W-Re TGA/DTA rod and furnace control thermocouple was used, along with $85\ \mu\text{L}$ W crucibles. The standard alumina furnace tube was replaced with an amorphous carbon tube. Approximately 80mg of powder was loaded into one W crucible, with the other crucible being left empty. The system was evacuated to $0.40\ \text{mbar}$ using a roughing pump and then filled with UHP helium at $200\ \text{mL}/\text{min}$. Once atmospheric pressure was achieved

in the furnace, helium flow was reduced to 20mL/min. Measurement was started after mass signal stabilized from change in flow rate. The furnace ramped at 15K/min to 150°C and dwelled for 20 minutes to ensure adsorbed moisture was gone. The furnace was then ramped 10K/min to 1000°C with the sample temperature overshooting by 7°C on average. After one hour hold at 1000°C in 20mL/min flowing helium, the gas flow was changed to 20mL/min 4% H₂ in argon. Dwell time at 1000°C was 16 or 40 hours.

Non-isothermal TGA measurements were done for each of the spinel compositions. Approximately 100mg of sample was loaded into one W crucible with the other remaining empty. The process of vacuum pumping and backfilling with helium was the same as isothermal TGA measurements. Flow rate of 20mL/min helium was set, and the furnace ramped at 15K/min to 200°C with a dwell time of 40 minutes to remove adsorbed water. The gas flow was then switched to 20mL/min of 4% H₂ in argon, and the furnace ramped at 2.5K/min to 1100°C.

b. Room Temperature X-ray Diffraction

X-ray diffraction was performed in Bragg-Brentano geometry on unreduced and reduced spinels using both thick mount powder specimens and zero-background holders. Patterns were obtained on a Bruker D8 Advance diffractometer using Cu-K α radiation, a 2.5° Soller slit, a 15 mm incident beam variable slit for thick mount specimens or 5mm incident beam variable slit for zero-background holders, 30 rotations per minute in-plane spinning, a Ni foil K β filter, and a LynxEye position sensitive detector with a range of 2.946° 2 θ , using a step size of 0.014° 2 θ , and a count time of 1 second from 10-100° 2 θ .

c. High Temperature X-ray Diffraction in Flowing 4% H₂/N₂

High temperature X-ray diffraction in flowing 4% H₂/N₂ was done in a custom Siemens D5000 diffractometer.⁹⁹ Cu-K α radiation was used with a Vantec-1 position sensitive detector with a range of 12° 2 θ . Samples were ground in an alumina mortar and pestle in isopropanol and deposited onto platinum coated sapphire sample holders. Scan parameters were 15 to 80° 2 θ with a scan rate of 5° 2 θ /minute. A step size of 0.2° 2 θ was used with a count time of 0.23s/step, for a time of 11 minutes and 5 seconds per pattern. 100 mL/min of flowing 4% H₂/N₂ was used throughout the measurement. The time-temperature profile included heating from room temperature to 200°C before heating in 100°C steps to 1000°C from 200°C and subsequently in

20°C steps to 1200°C, followed by cooling to room temperature. A measurement was taken at each step.

d. Standard Voltage Scanning Electron Microscopy

An FEI Quanta 200F Environmental Scanning Electron Microscope was used to collect all standard voltage electron micrographs. Samples were dispersed onto carbon planchets and carbon coated, unless they were considerably coated by carbon filaments already.

e. Catalysis Measurement

Catalyst selectivity was measured using a fixed bed quartz reactor by Nexceris.

C. Results and discussion

1. Powder Properties

The phases present following reduction include defect spinel, monoclinic and tetragonal ZrO_2 , and metal phases, as seen in Figure 2.

Bet

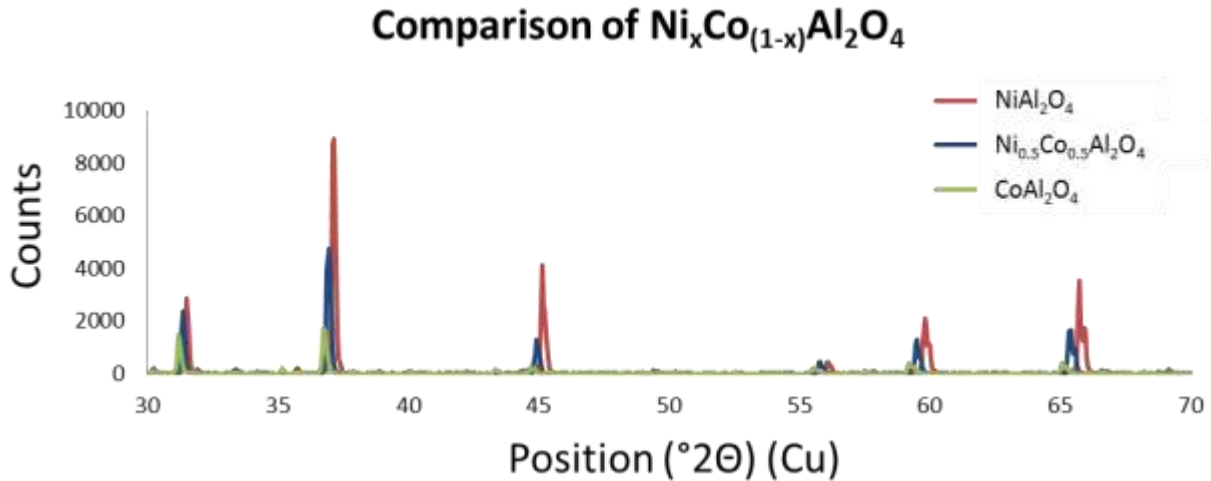


Figure 2. Comparison of the XRD data for three compositions calcined at $1500^{\circ}C$ for 8 hours and reduced at $800^{\circ}C$ for 8 hours.

In the case of $NiAl_2O_4$ reduced at $900^{\circ}C$, the spinel peak broadens and loses intensity as extent of calcination increases. In the case of the two Co-containing spinels reduced at $800^{\circ}C$, a similar trend is seen. (Figs. 3-5) The Ni metal peaks grow and narrow as extent of calcination increases. (Figs. 6-7)

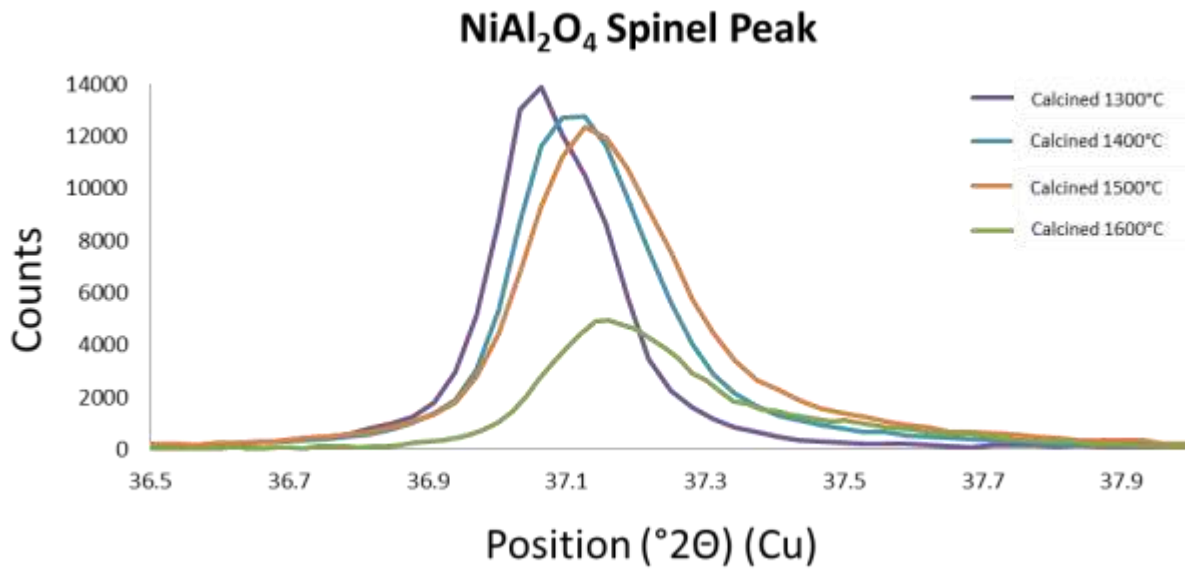


Figure 3. Spinel peak in NiAl₂O₄ calcined at 1300-1600°C and reduced at 900°C.

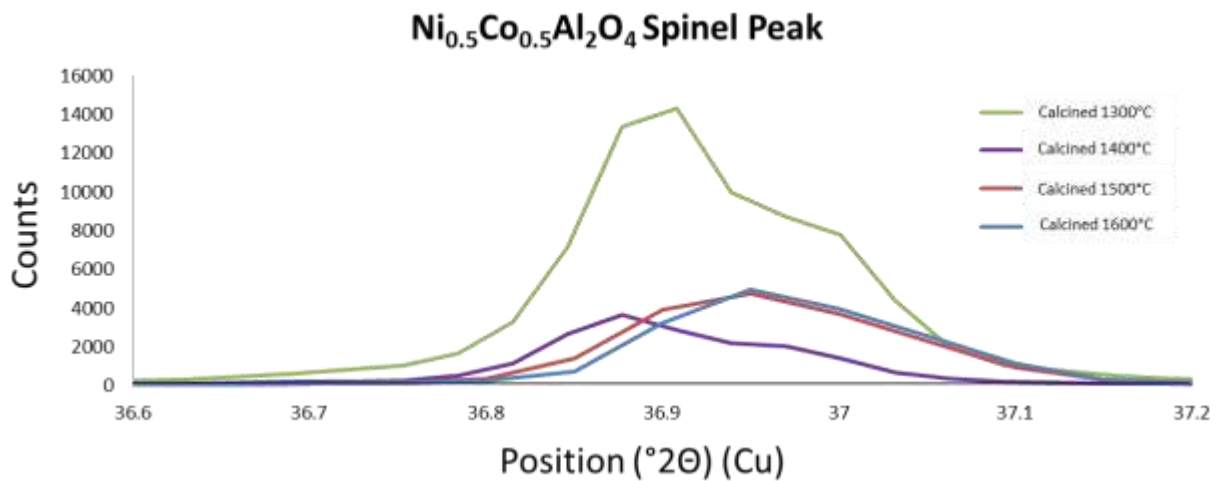


Figure 4. Spinel peak in Ni_{0.5}Co_{0.5}Al₂O₄ calcined at 1300-1600°C and reduced at 900°C.

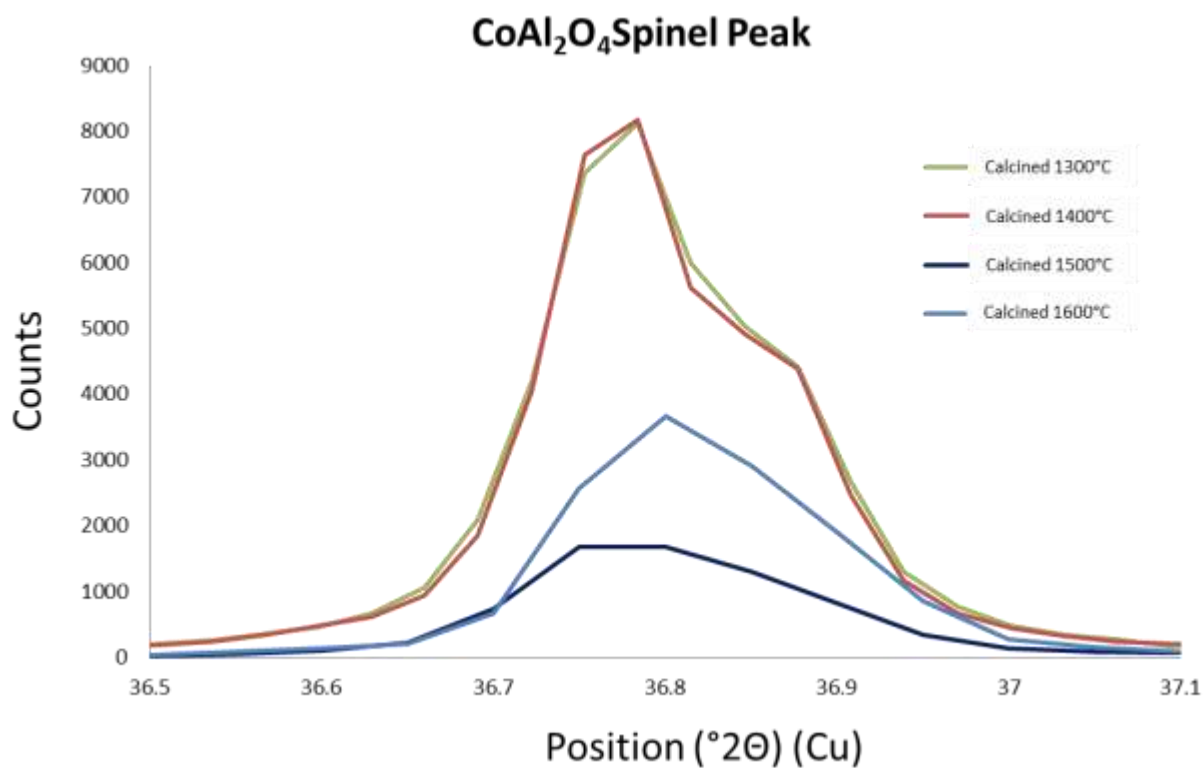


Figure 5. Spinel peak in CoAl₂O₄ calcined at 1300-1600°C and reduced at 900°C.

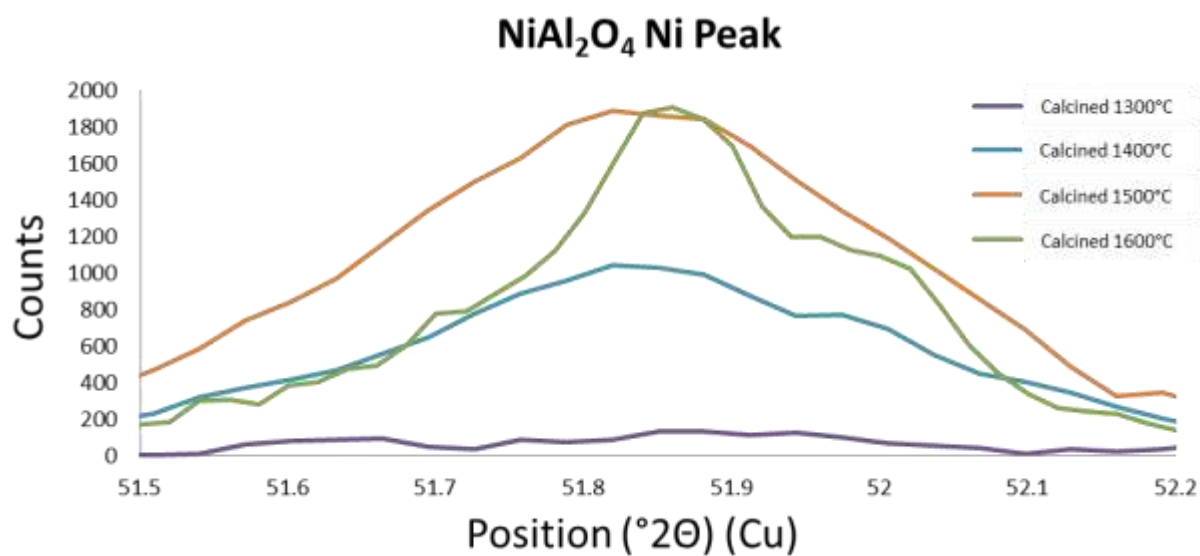


Figure 6. Metal peak in NiAl₂O₄ calcined at 1300-1600°C and reduced at 900°C.

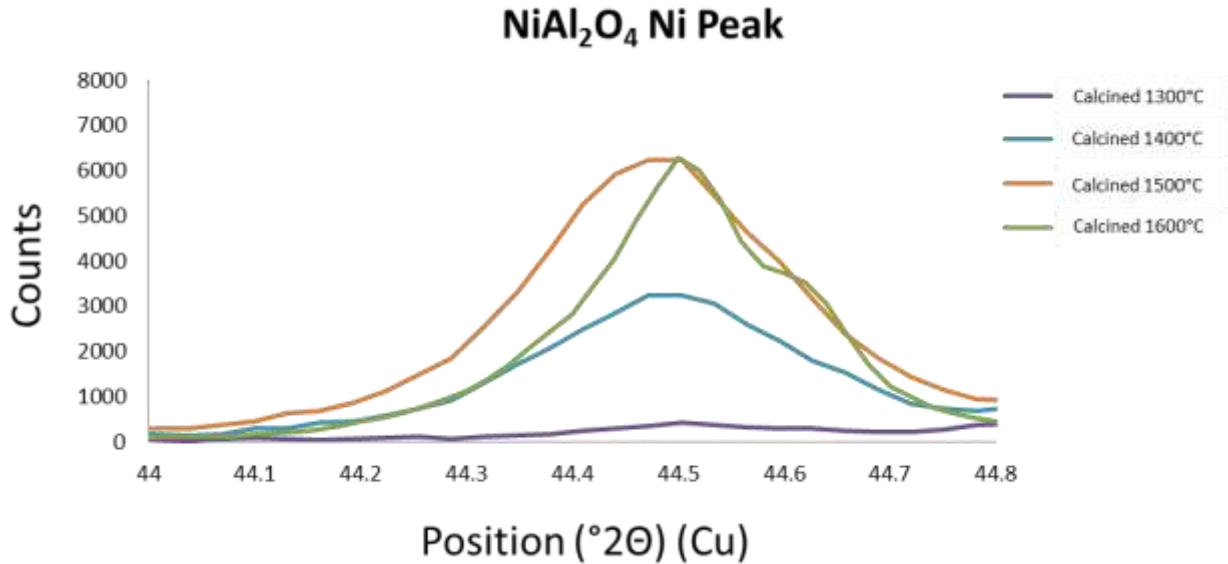


Figure 7. Metal peak in NiAl₂O₄ calcined at 1300-1600°C and reduced at 900°C.

During calcination, the morphology of the spinel phase changes dramatically. Many faceted, angular faces can be seen on the surface of the unreduced NiAl₂O₄, Ni_{0.5}Co_{0.5}Al₂O₄, and CoAl₂O₄ (Figs. 8-10). The ZrO₂ appears as large, spherical particles along the grain boundaries. The degree of faceting increases with increasing sintering temperature. When the spinel is reduced, small metal particles nucleate on the surface of the grains along the steps, as seen in Figs. 11 and 12. As reduction temperature increases, the size of the metal particles increases, as seen in Figs. 13-22. In Fig. 23, material is missing on the steps, which indicates outward mass transport of metallic cations occurring in that area during reduction. These cations form the metallic particles situated on the facets after reduction. The samples shown in Fig. 23 were reduced for 2 days in flowing 4% H₂/96% N₂ gas to coarsen the metal particles, which could have furthered the reduction of the sample leading to large pits in the support.

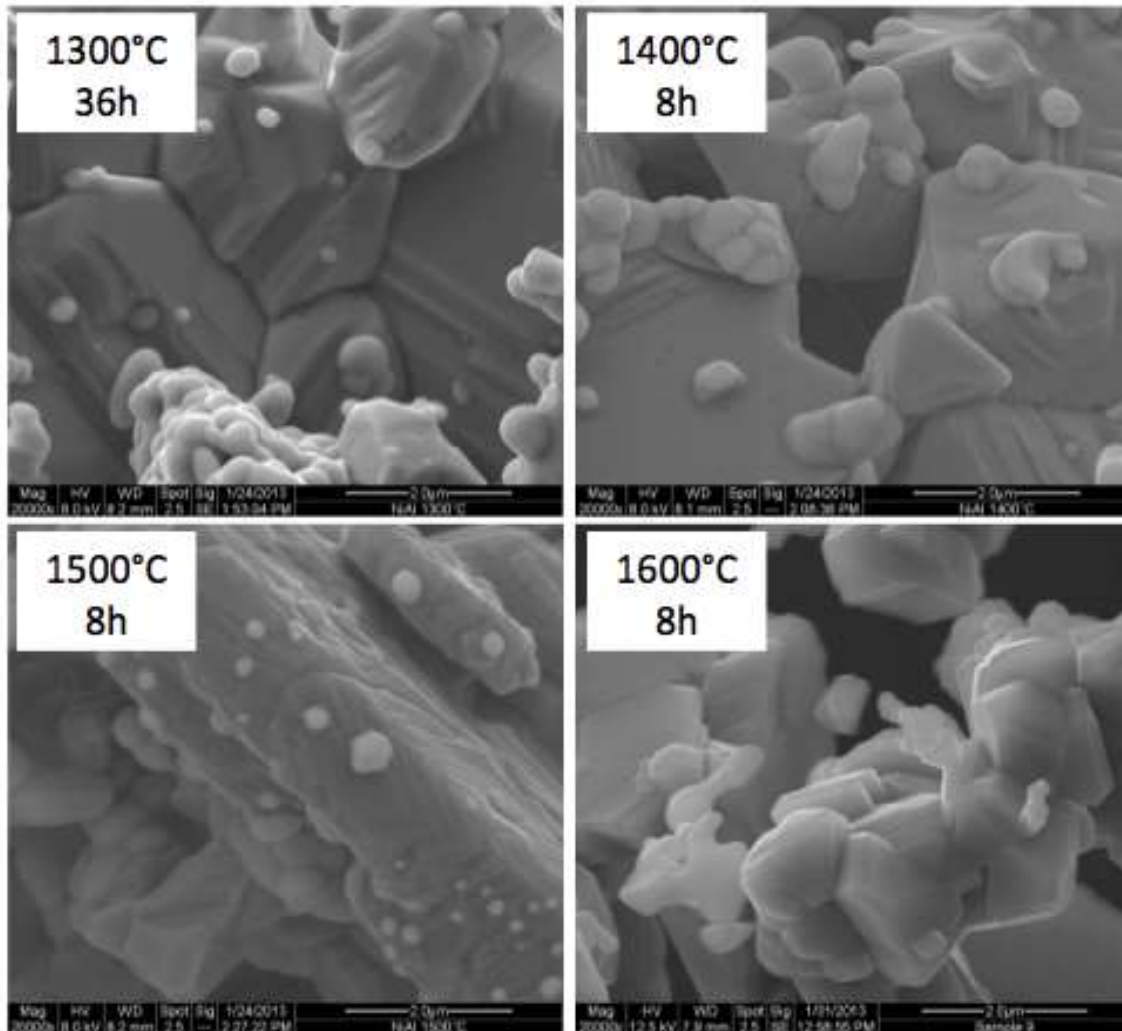


Figure 8. Change in degree of faceting in NiAl_2O_4 can be seen as calcination temperature increases.

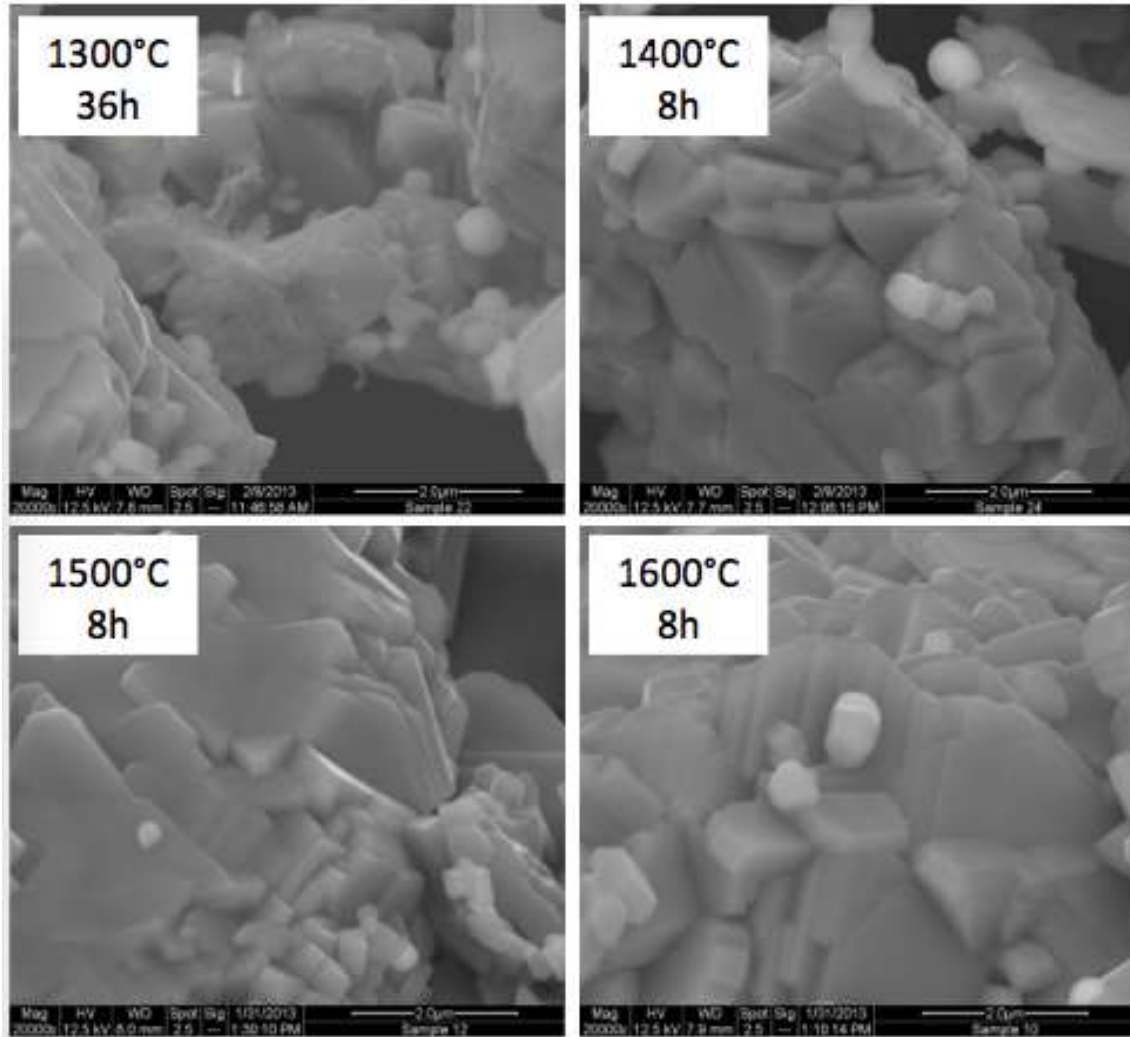


Figure 9. Change in degree of faceting in $\text{Ni}_{0.5}\text{Co}_{0.5}\text{Al}_2\text{O}_4$ can be seen as calcination temperature increases.

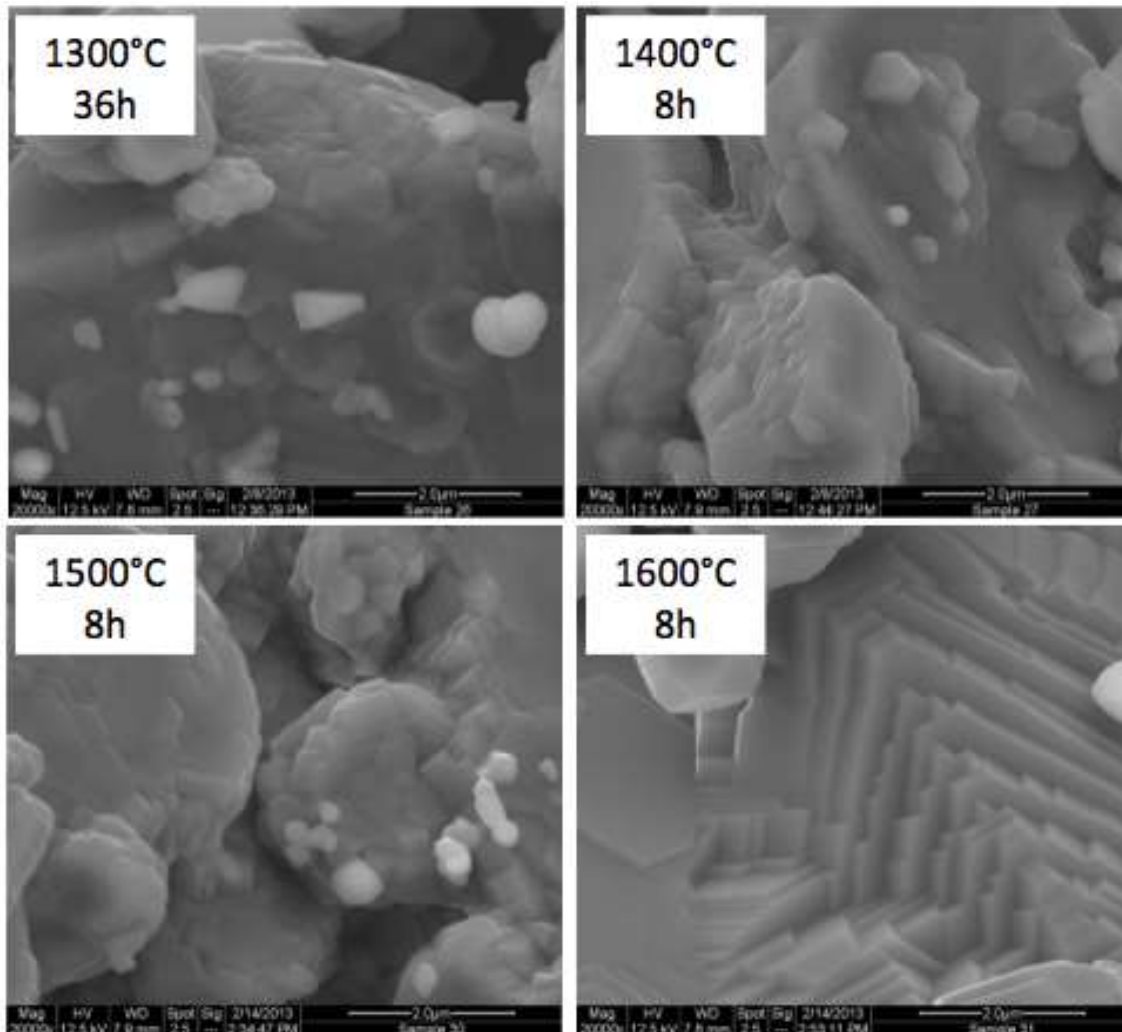


Figure 10. Change in degree of faceting in CoAl_2O_4 can be seen as calcination temperature increases.

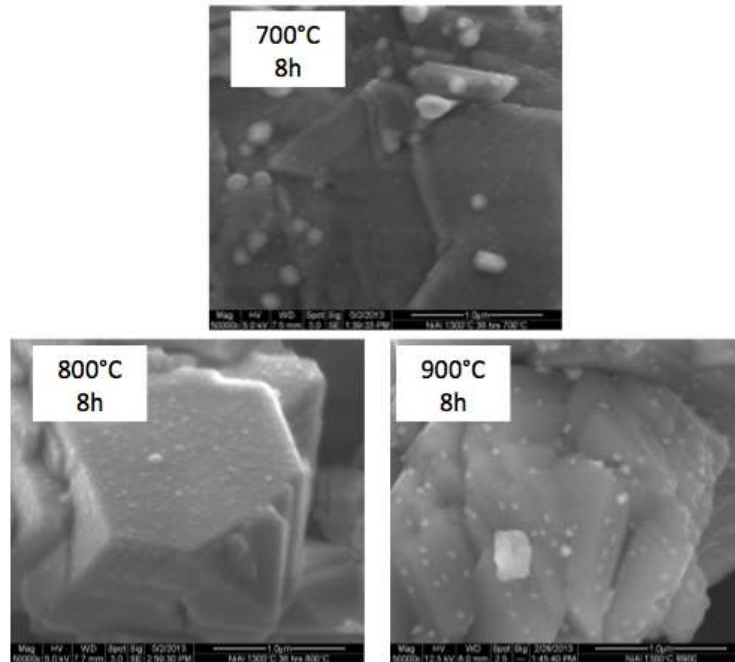


Figure 11. SEM showing increase in size of Ni metal particles with increasing reduction temperature for NiAl_2O_4 powders calcined at 1300°C for 36 hours.

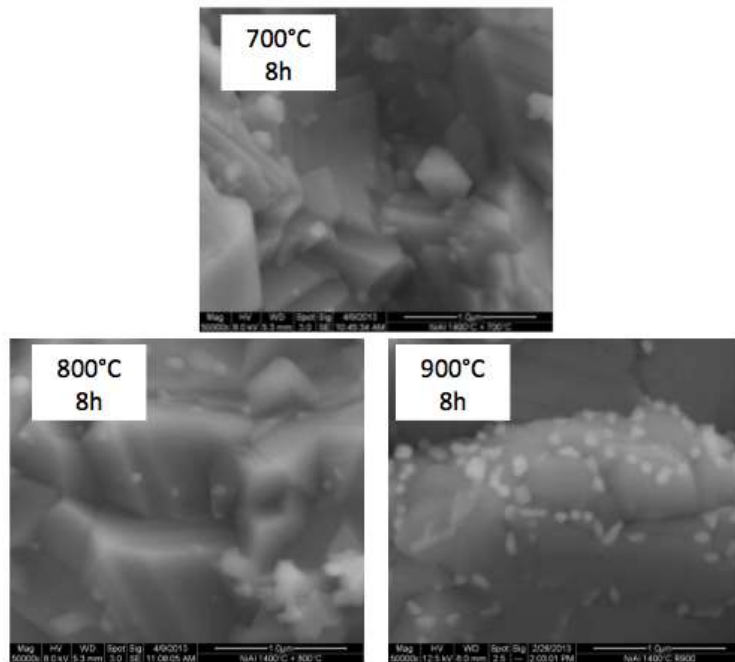


Figure 12. Increase in size of Ni metal particles with increase in reduction temperature on NiAl_2O_4 calcined at 1400°C for 8 hours.

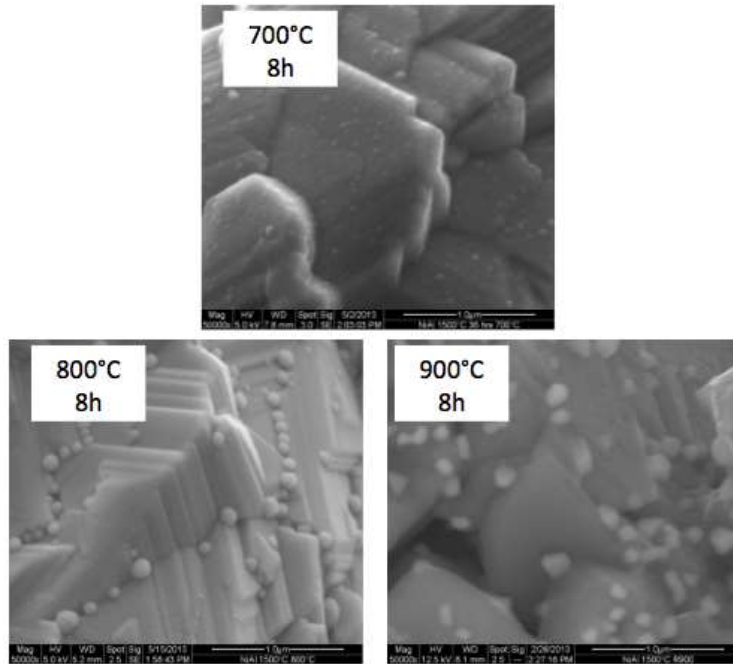


Figure 13. NiAl_2O_4 calcined at 1500°C for 8 hours and reduced at 700°C , 800°C , and 900°C for 8 hours.

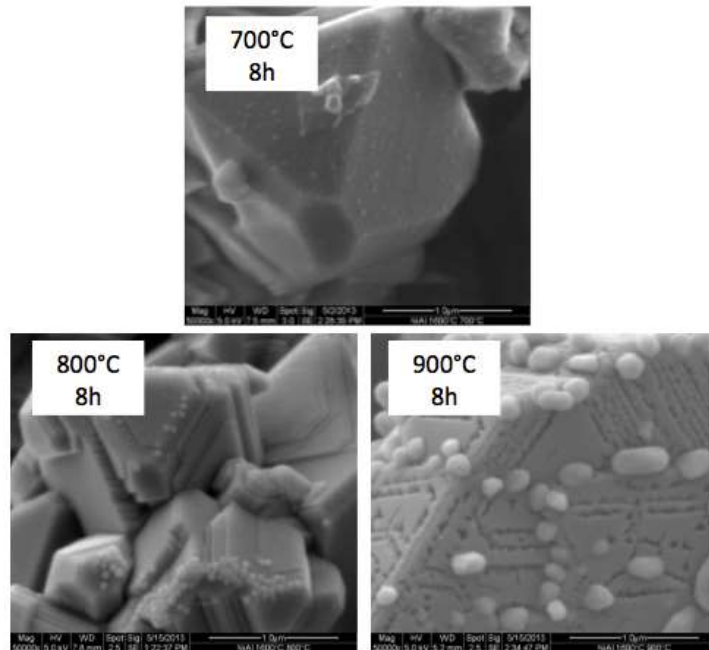


Figure 14. NiAl_2O_4 calcined at 1600°C for 8 hours and reduced for 8 hours at 700°C , 800°C , and 900°C .

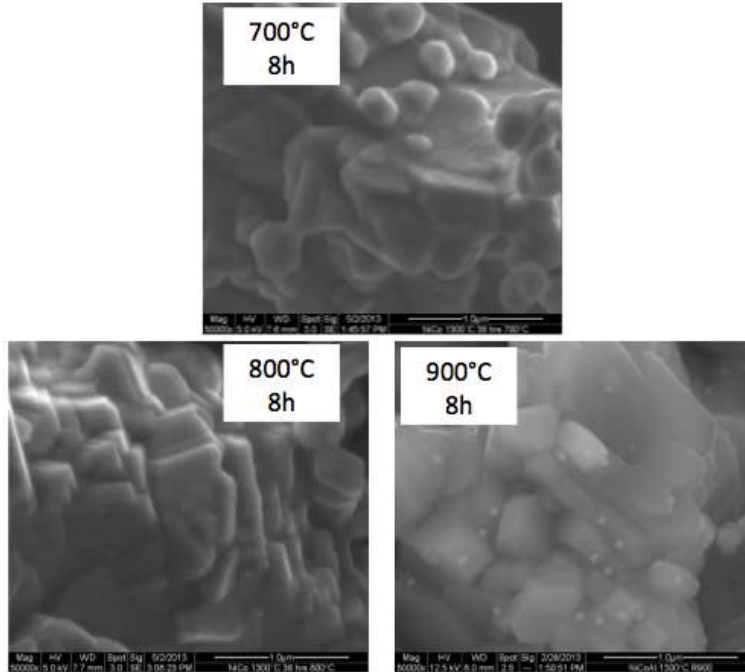


Figure 15. $\text{Ni}_{0.5}\text{Co}_{0.5}\text{Al}_2\text{O}_4$ calcined at 1300°C for 36 hours and reduced for 8 hours at 700°C , 800°C , and 900°C .

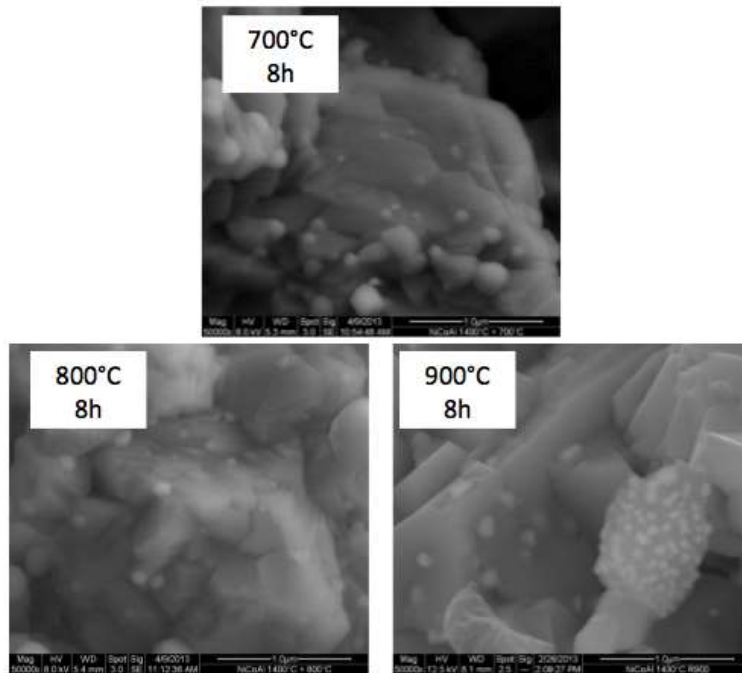


Figure 16. $\text{Ni}_{0.5}\text{Co}_{0.5}\text{Al}_2\text{O}_4$ calcined at 1400°C for 8 hours and reduced for 8 hours at 700°C , 800°C , and 900°C .

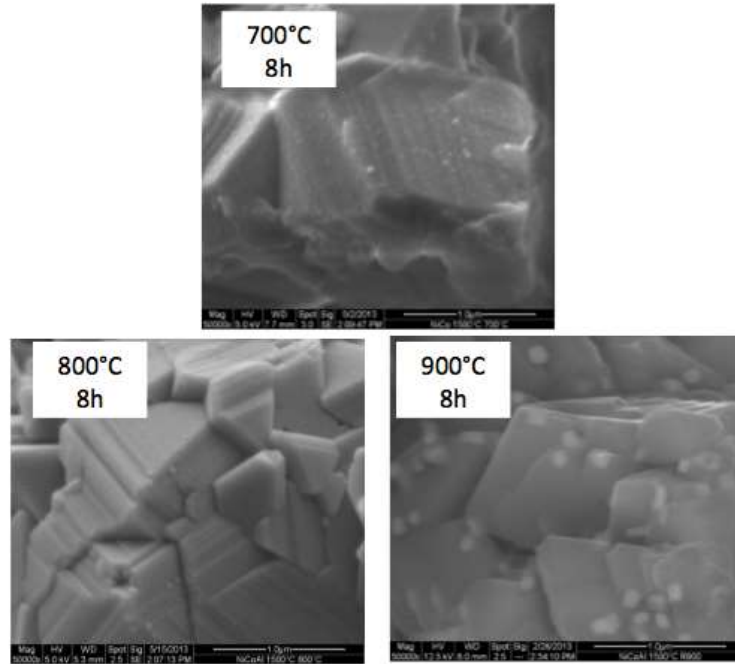


Figure 17. $\text{Ni}_{0.5}\text{Co}_{0.5}\text{Al}_2\text{O}_4$ calcined at 1500°C for 8 hours and reduced for 8 hours at 700°C , 800°C , and 900°C

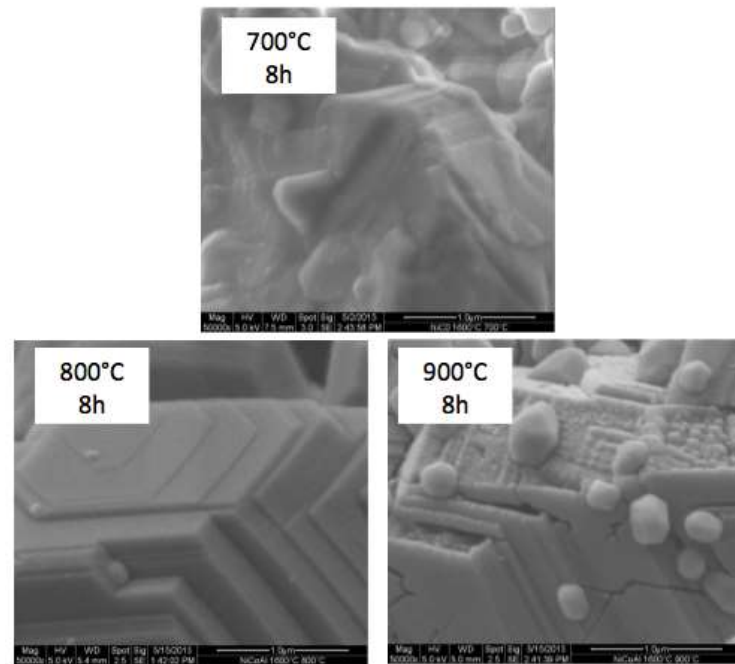


Figure 18. $\text{Ni}_{0.5}\text{Co}_{0.5}\text{Al}_2\text{O}_4$ calcined at 1600°C for 8 hours and reduced for 8 hours at 700°C , 800°C , and 900°C

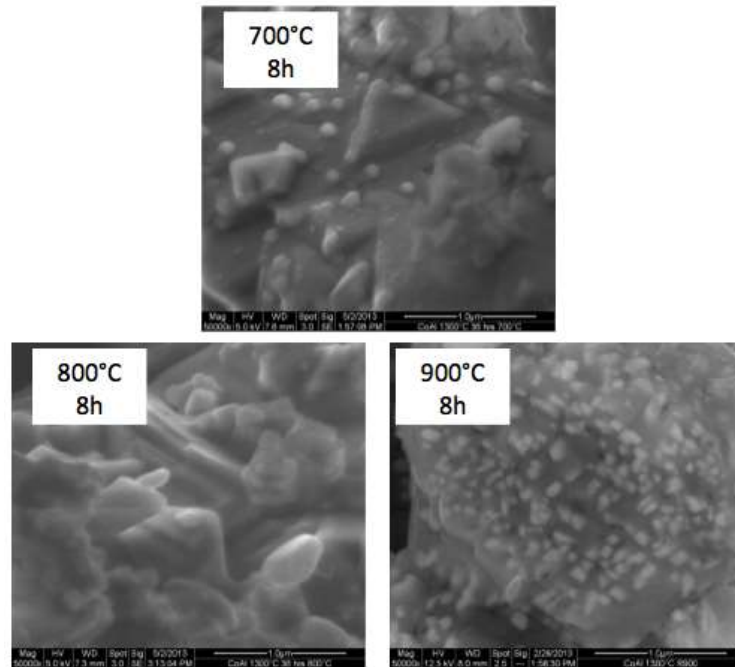


Figure 19. CoAl_2O_4 calcined at 1300°C for 36 hours and reduced for 8 hours at 700, 800, and 900°C .

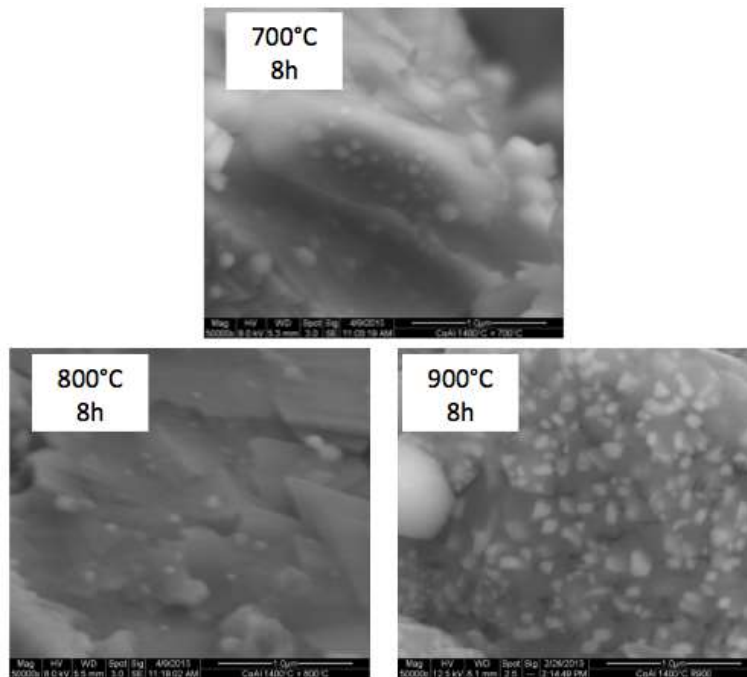


Figure 20. CoAl_2O_4 calcined at 1400°C for 8 hours and reduced for 8 hours at 700, 800, and 900°C .

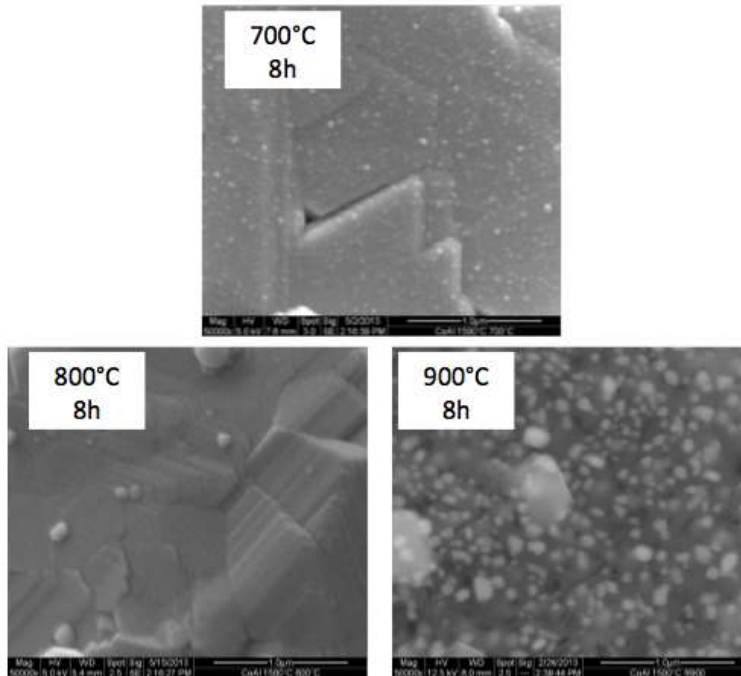


Figure 21. CoAl_2O_4 calcined at 1500°C for 8 hours and reduced for 8 hours at 700, 800, and 900°C .

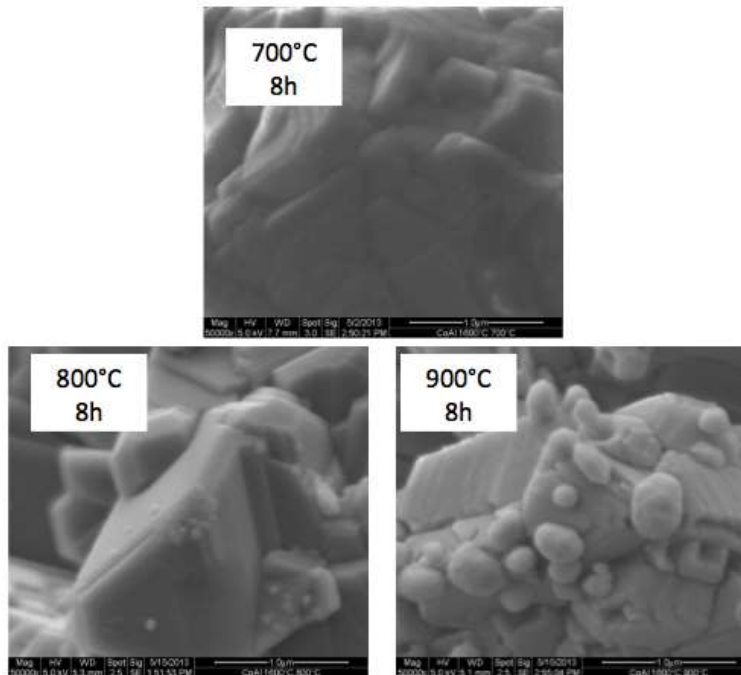


Figure 22. CoAl_2O_4 calcined at 1600°C for 8 hours and reduced for 8 hours at 700, 800, and 900°C .

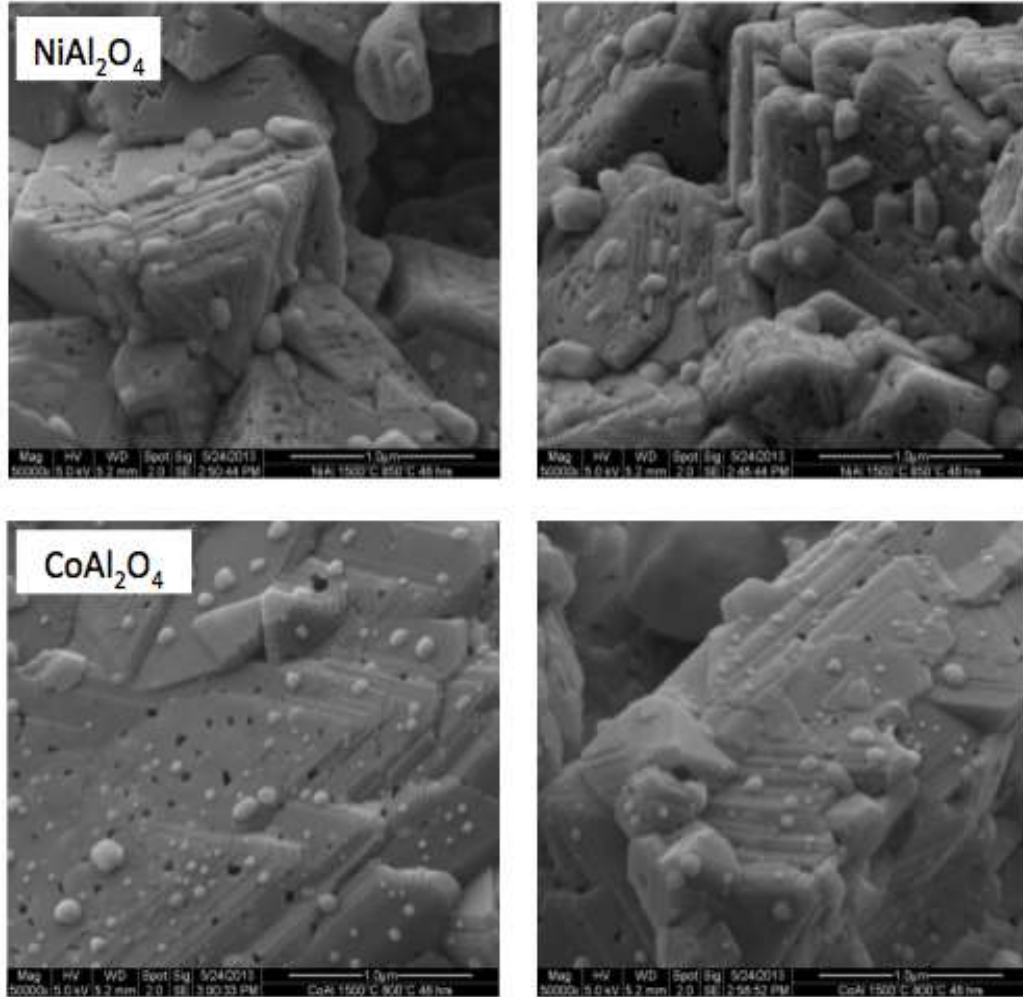


Figure 23. Ni- and Co- Al_2O_4 spinels calcined at 1500°C for 8 hours and reduced in $4\% \text{H}_2/96\% \text{N}_2$ for 48 hours.

2. Reduction Kinetics (TGA/HTXRD)

Several isothermal and non-isothermal TGA measurements were done in reducing atmosphere to study kinetics and check for correlation in reduction temperature between HTXRD and TGA. It is necessary to reduce the A-site cations (seen in Figure 24) enough to provide sites for catalysis, while still retaining a defect spinel structure. In other words, it is important not to over-reduce the sample by using a high reduction temperatures and/or long reduction times. The coefficient of thermal expansion of the reduced samples was important as composite CTE of the anode material needed to closely match that of the YSZ electrolyte support.

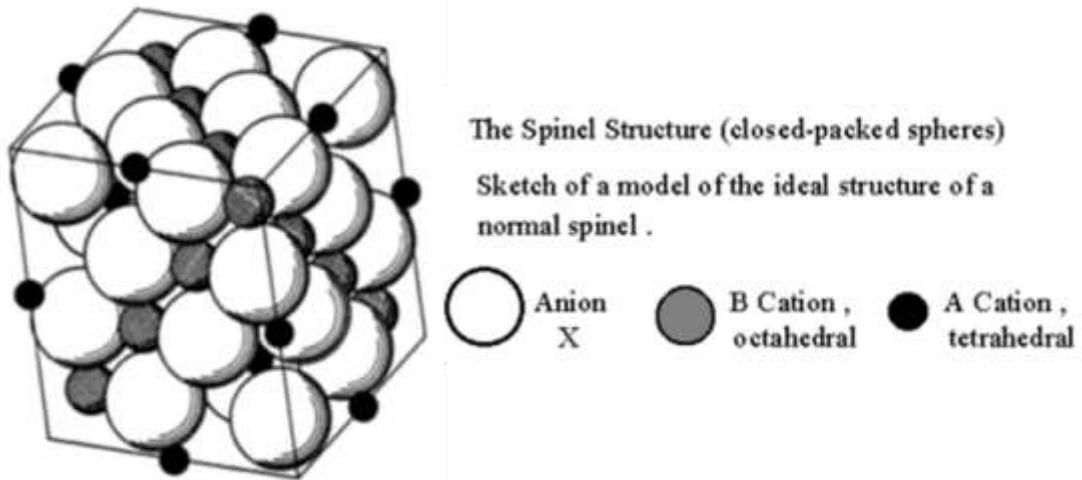


Figure 24. Drawing of spinel structure showing positions of A-site and B-site cations in the unit cell.¹¹³

A change in the lattice constant of the spinel occurs during the reduction process (Figs. 25-26).¹⁰⁰ As the spinel is reduced, the metallic ions Ni and Co are removed from the spinel structure to form metal particles on the surface supported by a defect spinel. This information was used to calculate the CTE of the defect spinel support and the metallic nanoparticles, as seen in Table 2.

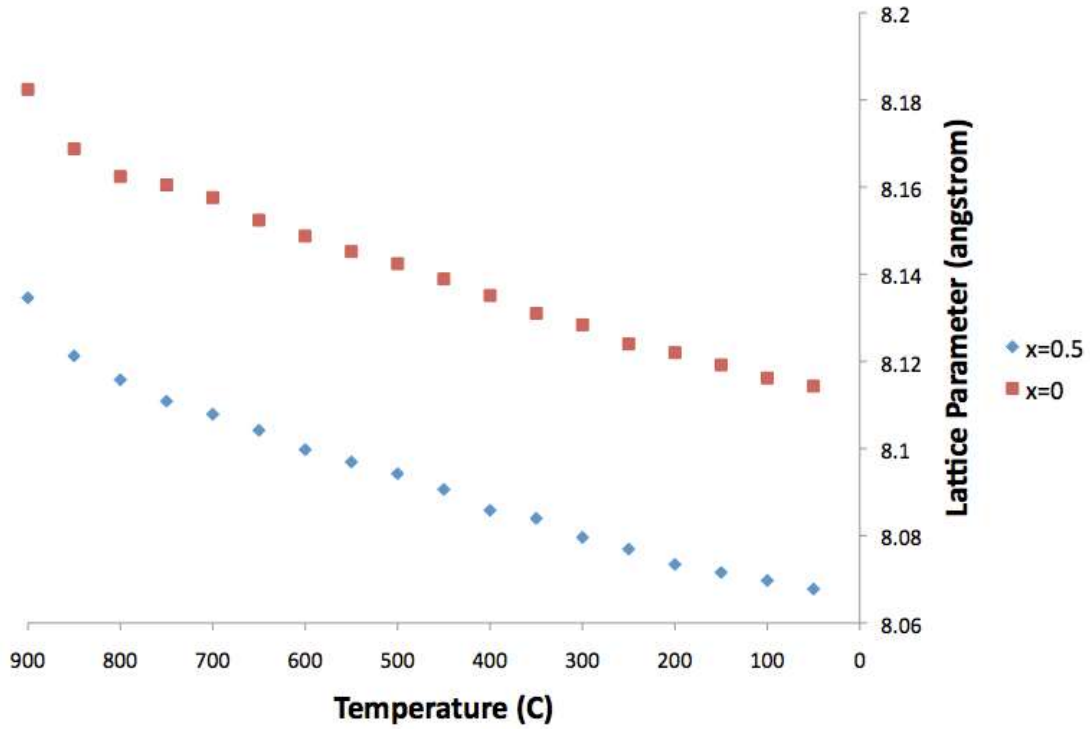


Figure 25. Lattice parameter of the defect spinel support for $Ni_xCo_{(1-x)}Al_2O_4$ with decrease in temperature.

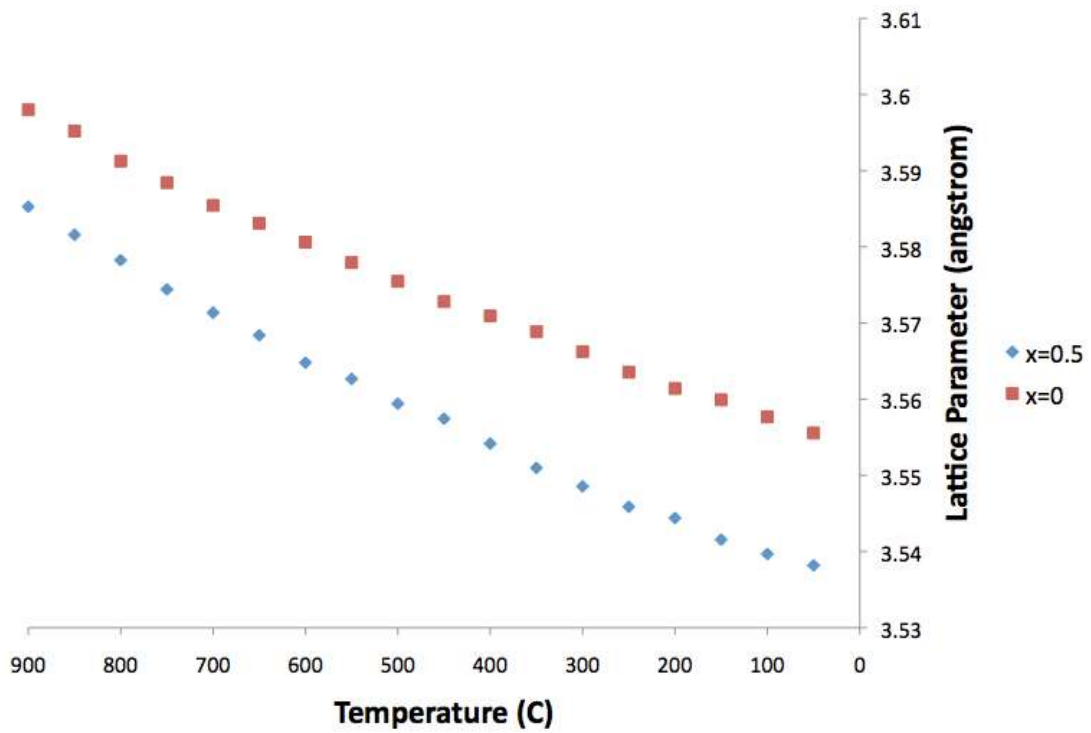


Figure 26. Lattice parameter of metallic nanoparticles for $Ni_xCo_{(1-x)}Al_2O_4$ with decrease in temperature.

Table 2. Coefficients of Thermal Expansion of Defect Spinel and Metals from HTXRD Pattern Refinement.

		CTE (/T)	
		Spinel	Metal
Composition	x=1	8.28E-06	3.39E-06
	x=0.5	9.83E-06	1.59E-05
	x=0	9.95E-06	1.43E-05

There is also a clearly defined metal peak shift in the XRD patterns as Co content increases, seen in Figure 27. The XRD peak shape of the Ni metal has a low-angle shoulder that is refined well with the addition of a hat function convolution factor. The hat function magnitude decreases with increasing temperature, which indicates strain due to thermal expansion mismatch between the Ni metal particles and the support.¹¹¹ This potentially indicates a close bond between metal and spinel support, which can prevent coarsening behavior of the metal and subsequent catalyst deactivation.¹⁰¹ NiAl₂O₄ has been shown to interact strongly with Ni, resulting in interfacial bonding between the catalyst and its support. In addition to preventing agglomeration, it can also prevent premature oxidation.^{102,103} Anchoring has also been seen between Ni metal and ceria supports, with certain planes of ceria anchoring the metal better than others.¹⁰⁴ Neutron diffraction can be used to further analyze internal strain as neutrons have an increased penetration depth compared to x-rays. The elastic strain can then be determined by the change in lattice spacing versus a calculated condition without strain present.²⁴ The reduction of Ni⁰ out of NiAl₂O₄ may lead to this strain, while the conventional wet impregnation approach may not. Lopez-Fonseca reported that Ni metal supported on NiAl₂O₄ catalyst outperformed the Ni/Al₂O₃ samples.¹⁰⁵ A possible cause for the strain could be that the Ni metal is nucleating on the surface on the defect spinel in a metastable crystal structure and slowly forming the more stable FCC structure as the Ni metal particle grows outward.¹⁰⁶

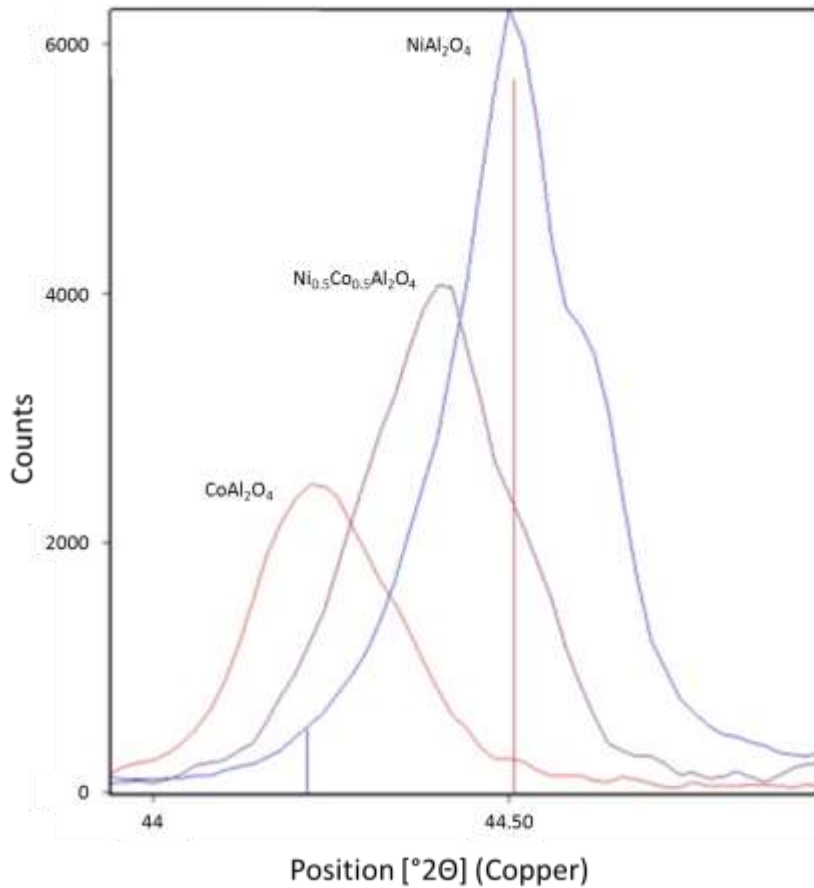


Figure 27. Metal peak shift between the three Ni- and Co- containing spinel samples, each calcined for 8 hours at 1600°C and reduced at 900°C for 8 hours in flowing hydrogen.

TGA analysis of the aluminate and ferrite spinels show the weight change associated with reduction, as seen in Figure 28. The ferrite spinels begin reducing well below standard operating temperatures for SOFCs and are over-reduced before operating temperatures are reached. Figure 29 shows the isothermal reduction of the aluminate spinels with a calculated reduction limit line included. All of the aluminate spinels approach this limit and then plateau at around 6 hours.

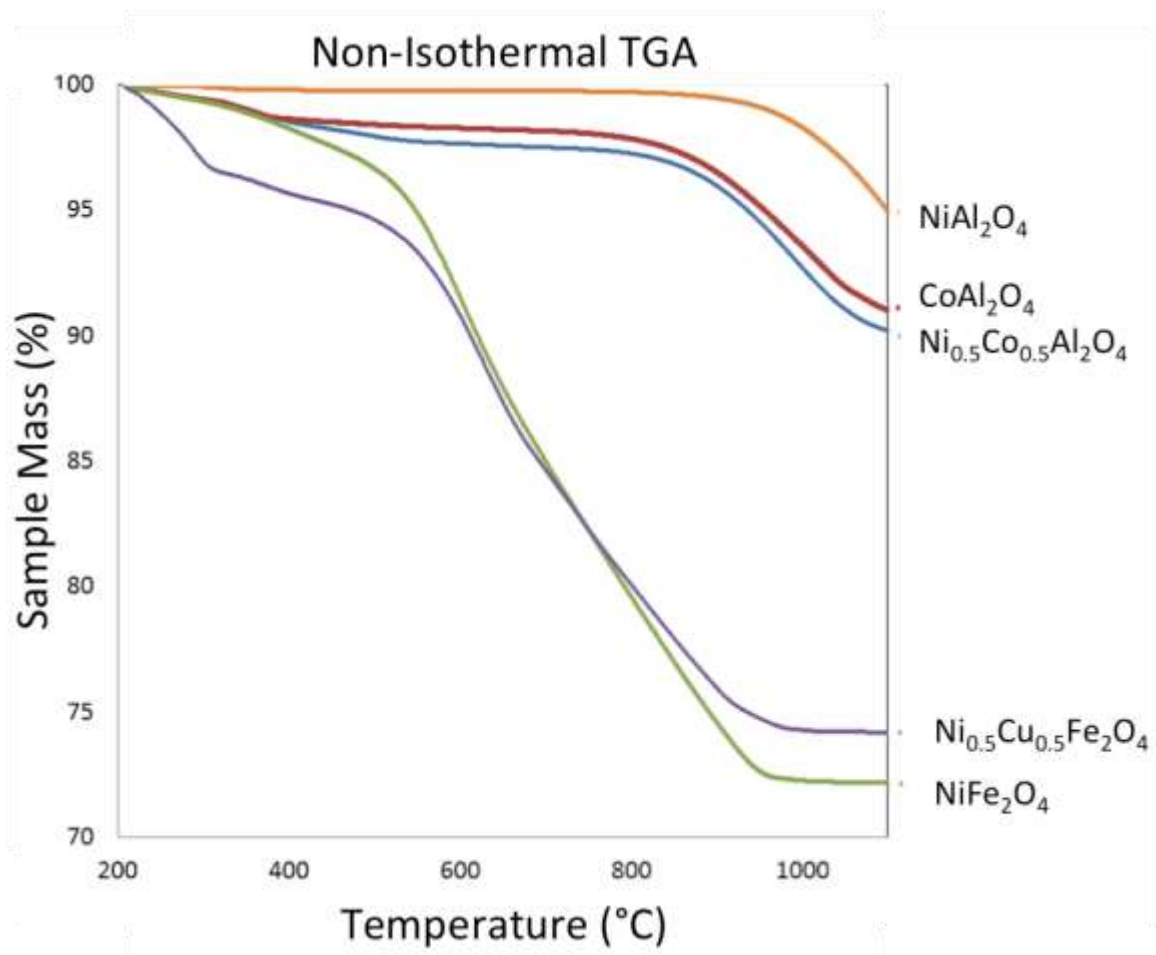


Figure 28. TGA analysis of aluminate and ferrite spinels.

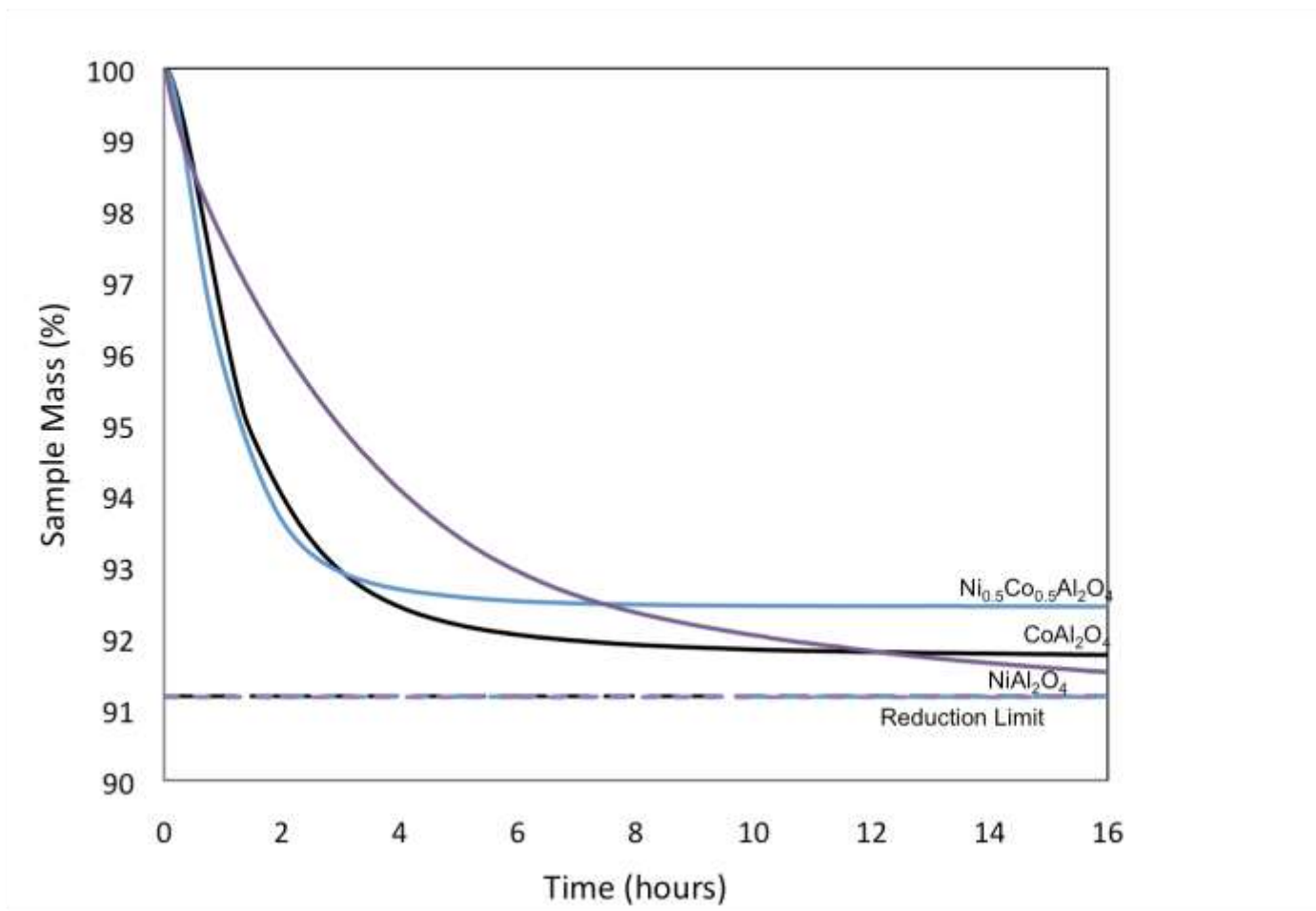


Figure 29. TGA data with reduction limits calculated by determining the sample mass lost if all Ni and/or Co present in the sample is reduced.

3. Oxidation/Reduction Cycling

In-situ x-ray diffraction (HTXRD) was done to show the reaction mechanisms involved during reduction and reoxidation. Figure 30 shows shows reduction of $\text{Ni}_{0.5}\text{Co}_{0.5}\text{Al}_2\text{O}_4$ with loss of spinel peaks starting at 900°C and ending at 1000°C , with appearance of NiCo alloy at 900°C . The reoxidation process, shown in Figure 31, shows that NiCo peaks gradually disappear starting around 500°C , but spinel peaks start forming later, closer to 1000°C , indicating formation of NiO and CoO prior to formation of spinel. This shows that while reduction must occur around 1000°C , reoxidation occurs slightly lower, at 800°C .

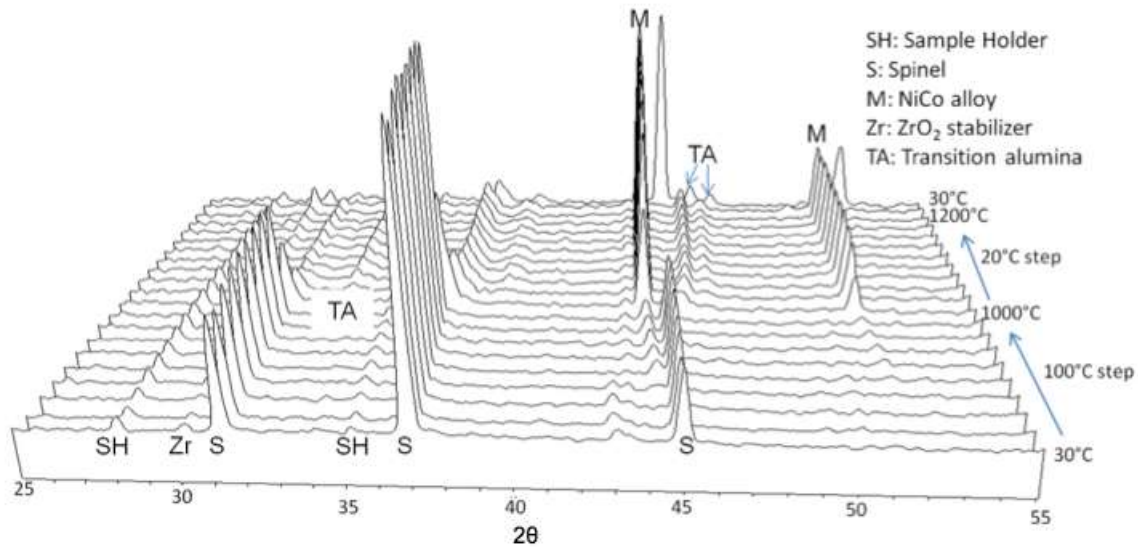


Figure 30. HTXRD patterns for the reduction of $\text{Ni}_{0.5}\text{Co}_{0.5}\text{Al}_2\text{O}_4$ to 1200°C .

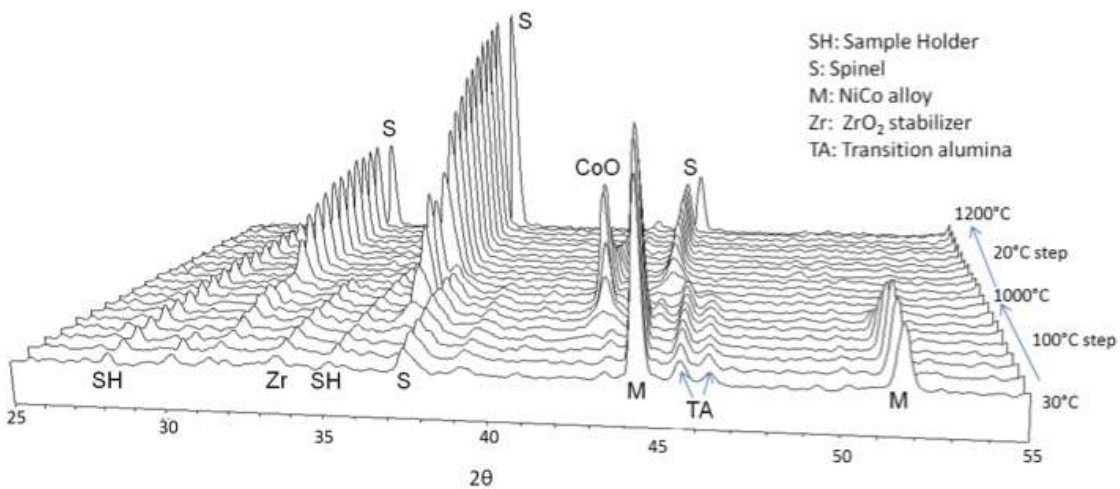


Figure 31. HTXRD patterns for reoxidation of $\text{Ni}_{0.5}\text{Co}_{0.5}\text{Al}_2\text{O}_4$ to 1200°C .

The small diffusional interface during spinel reversible transition from Co to CoAl_2O_4 causes spinel peaks to be broad initially, but they sharpen and grow as temperature increases (Fig 32). The 0.02Å peak shift to lower angle as temperature increases is caused by the difference in lattice parameter between the two phases.

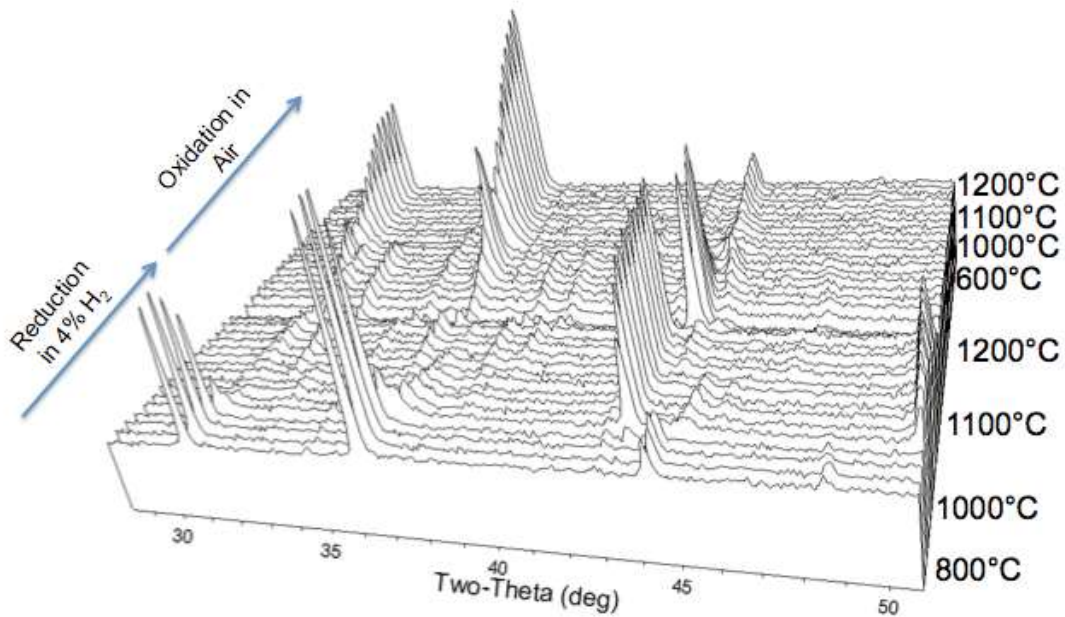


Figure 32. HTXRD patterns showing reduction and reoxidation of CoAl_2O_4 .

Repeated cycling done on $\text{Ni}_{1.5}\text{Co}_{0.5}\text{Al}_2\text{O}_4$ shows that there is no degradation in the spinel phase compositions after several cycles (Fig 33). However, the SEM images of NiAl_2O_4 and CoAl_2O_4 samples over 1 cycle (Fig. 34) show a significant change in morphology after the re-reduction process. This could be due to the fact that the initial reduction was carried out for 2 days, leading to the possibility of over-reduction and subsequent structure degradation.

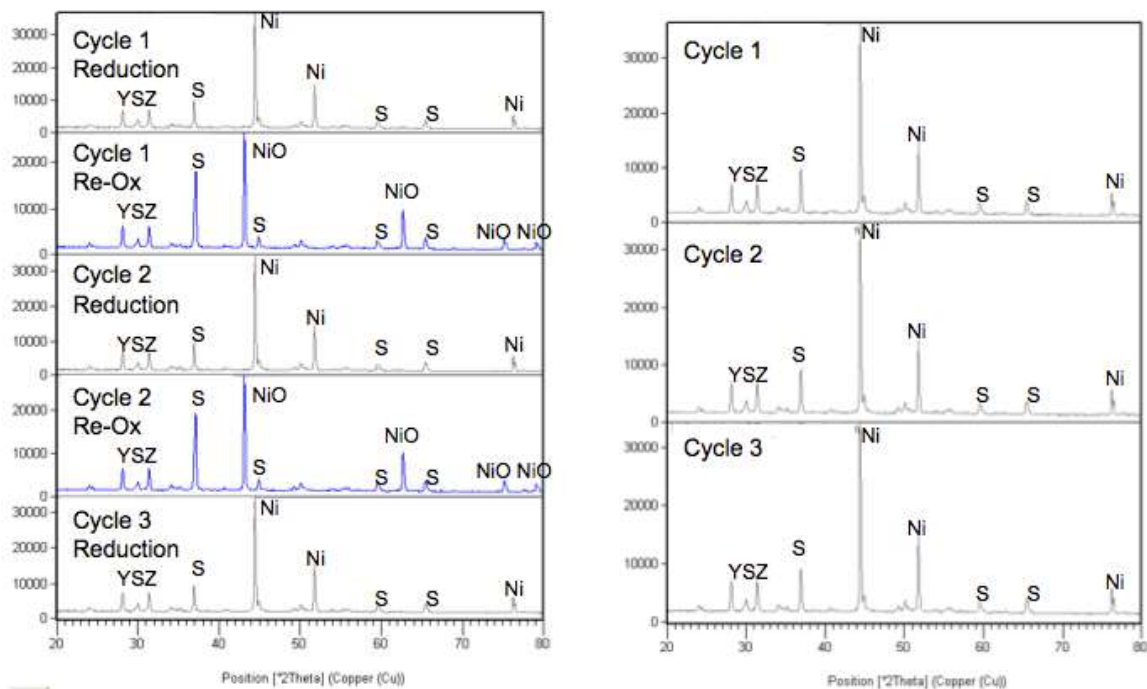


Figure 33. XRD patterns of $\text{Ni}_{0.5}\text{Co}_{0.5}\text{Al}_2\text{O}_4$ spinel over 3 cycles, showing no degradation in phase composition over the 3 cycles.

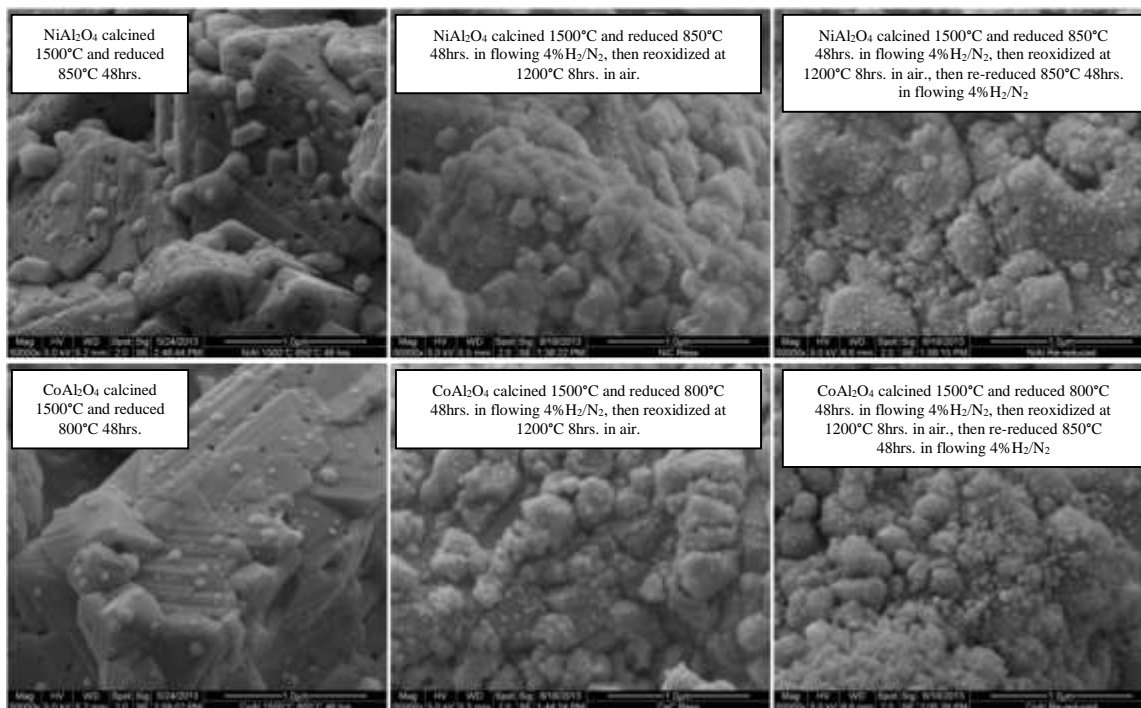


Figure 34. SEM images showing initial reduction with significant coarsening, reoxidation, and re-reduction of NiAl_2O_4 and CoAl_2O_4 samples.

4. Catalysis Studies

Several catalysis tests were done using the spinels by Nexceris. Using a gas composition of 47.5% CH₄, 47.5% CO₂, 5.0% N₂ and GHSV = 3,000 hr⁻¹, significant coking occurred within 1 hour at 850°C as evidenced by the increase in pressure drop within the reactor. In order to prevent coking, the gas composition was changed to 32.5% CH₄, 64.5% CO₂ and 3.0% N₂. GHSV increased to 6,000hr⁻¹ to decrease conversion below 100%. The performance of the Ni_{0.5}Mg_{0.5}Al₂O₄ catalyst didn't change during the 16 hours of testing and pressure drop didn't increase, indicating that deactivation by coking was not occurring (Fig. 35). The NiAl₂O₄ catalyst (Fig. 36) behaved similarly, but the Co- containing sample (Fig. 37) had a lower activity than the Ni-based spinels and lost activity over time.

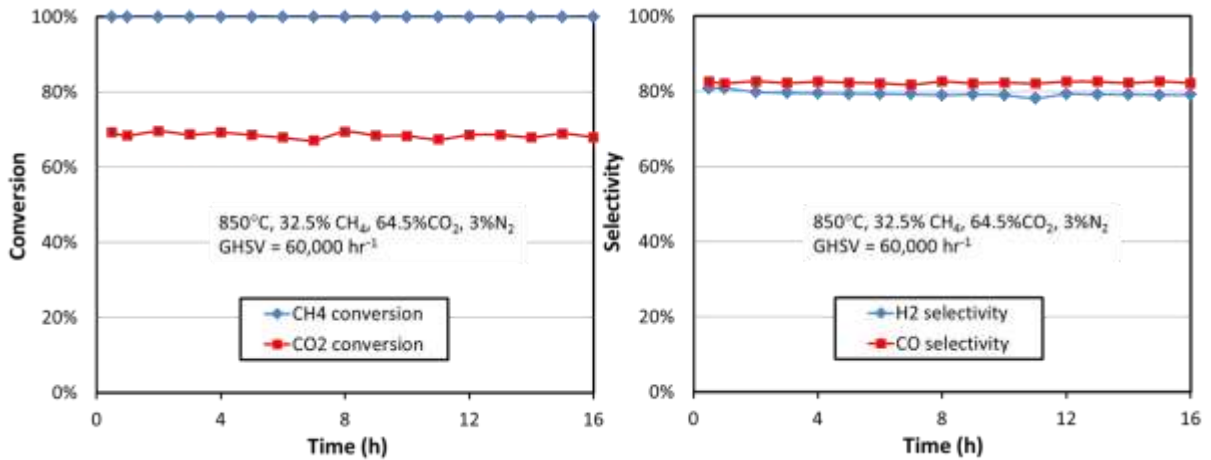


Figure 35. Methane reforming performance on Ni_{0.5}Mg_{0.5}Al₂O₄ catalyst under the conditions of 850°C, 32.5% CH₄, 64.5% CO₂, 3.0% N₂ and GHSV = 60,000 hr⁻¹.

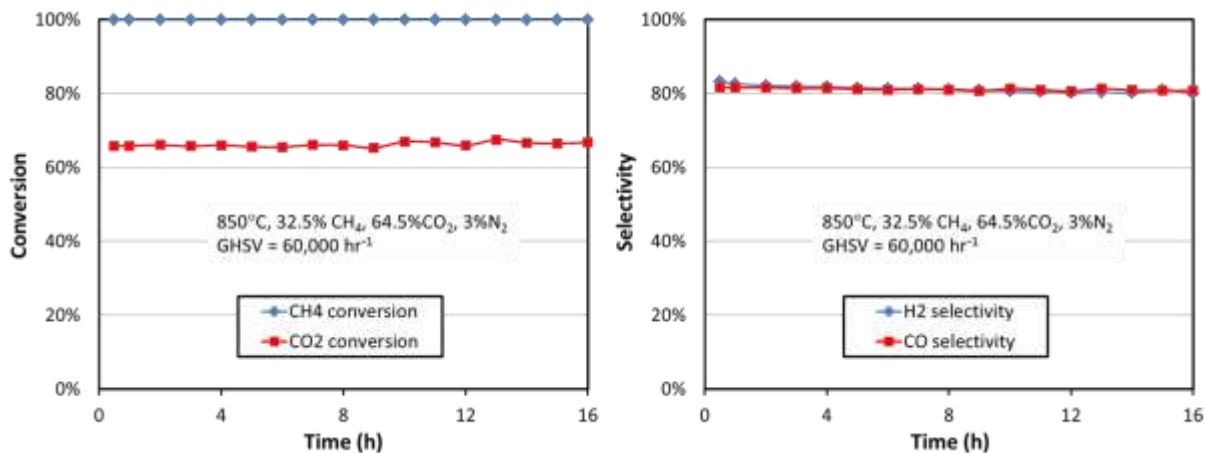


Figure 36. Methane reforming performance on NiAl₂O₄ catalyst under the conditions of 850°C, 32.5% CH₄, 64.5%CO₂, 3.0% N₂ and GHSV = 60,000 hr⁻¹.

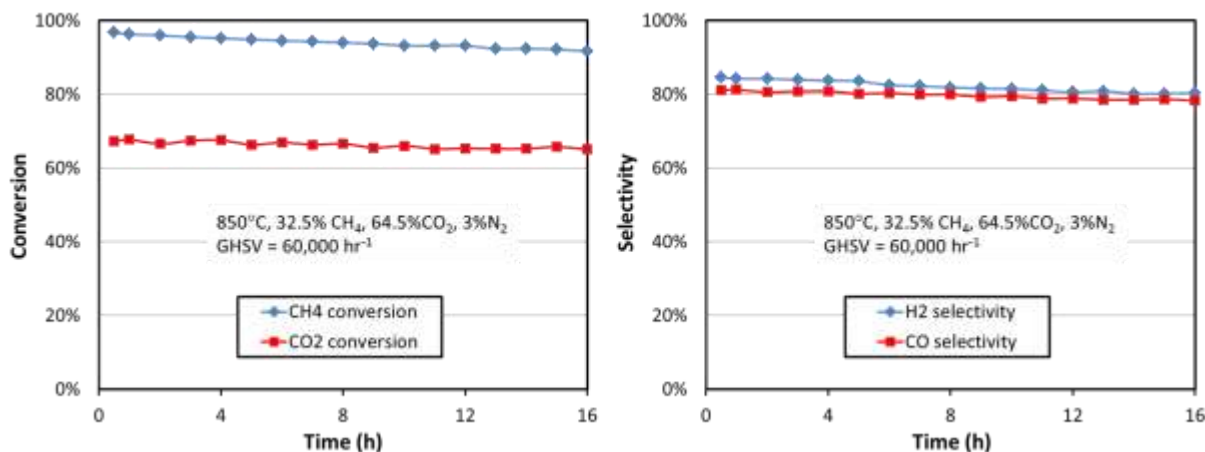


Figure 37. Methane reforming performance on Ni_{0.5}Co_{0.5}Al₂O₄ catalyst under the conditions of 850°C, 32.5% CH₄, 64.5%CO₂, 3.0% N₂ and GHSV = 60,000 hr⁻¹.

Further studies carried out by Nexceris tested the effect of temperature and sulfur on methane reforming performance for highly faceted NiAl₂O₄ and less faceted NiAl₂O₄. The temperature effect run was done between 650-850°C, 32.5% CH₄, 64.5% CO₂ 3.0% N₂ and GHSV = 60,000 hr⁻¹. To test the effect of sulfur, 20 ppm of H₂S/N₂ was added to the feed gas with a flow rate of 200mL/min. The less faceted catalyst conversions increased with reaction temperature. Methane conversion almost reached 100% at 850°C (Fig. 38). The conversion was slightly lower than for the more faceted sample (Fig. 39).

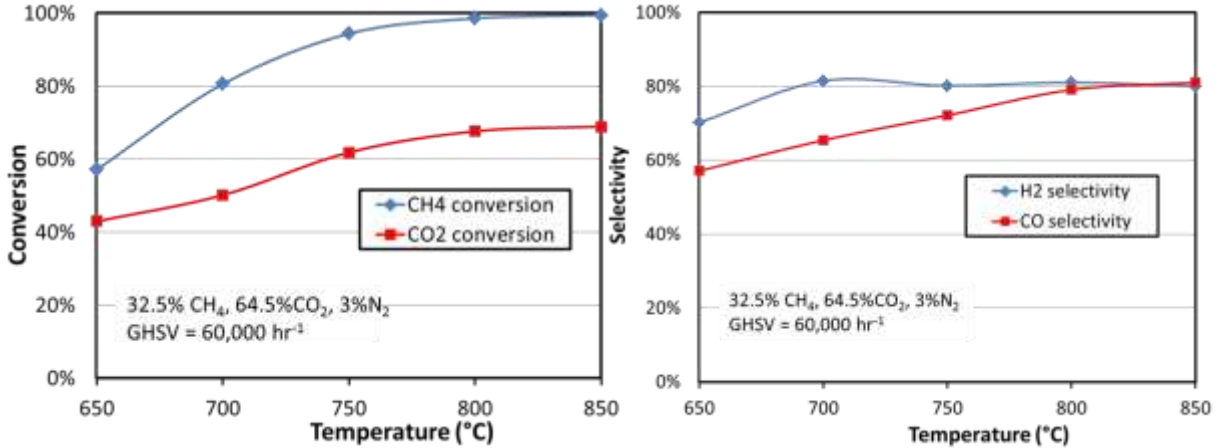


Figure 38. Methane reforming performance on NiAl₂O₄ (LT) catalyst under the conditions of 650-850°C, 32.5% CH₄, 64.5% CO₂, 3.0% N₂ and GHSV = 60,000 hr⁻¹.

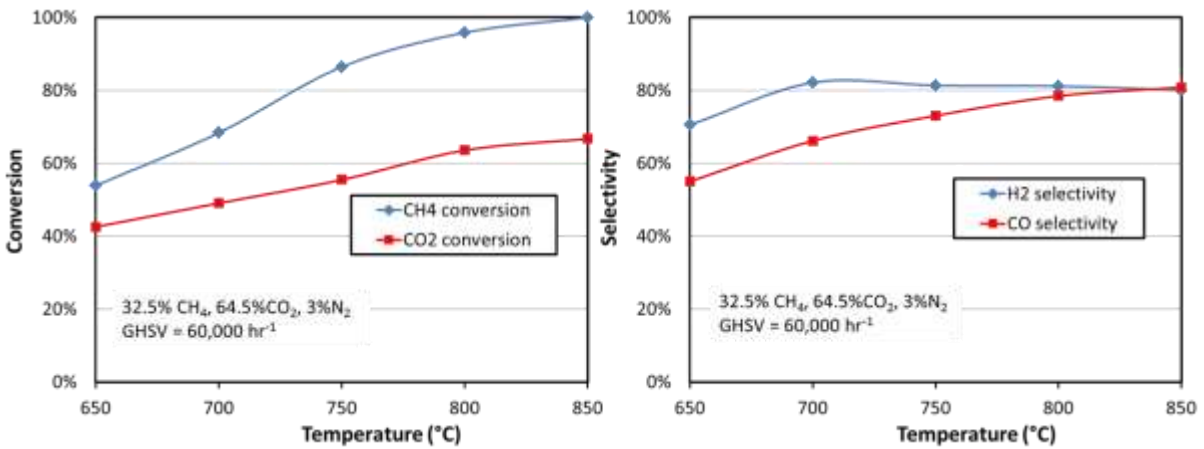


Figure 39. Methane reforming performance on NiAl₂O₄ catalyst under the conditions of 650-850°C, 32.5% CH₄, 64.5% CO₂, 3.0% N₂ and GHSV = 60,000 hr⁻¹.

The addition of H₂S to the feed gas at 850°C had a negative effect on the catalytic activity (Figs 40-41). The methane conversion nearly reached 100% initially for both catalyst, but decreased with time on stream. Methane and CO₂ conversion reduced to zero after 6 and 12 hours on the less faceted and more faceted catalysts, respectively. The deactivation is attributed to the sulfur poisoning, or chemical bonding of sulfur with catalytic sites, since deactivation doesn't occur without sulfur addition to feed gas. The highly faceted sample seems to withstand sulfur more than the less faceted one.

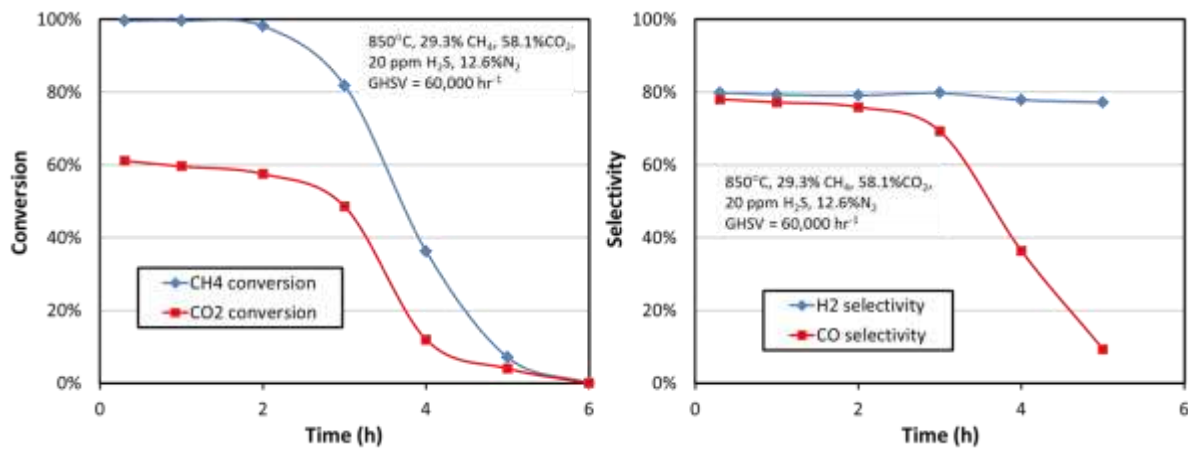


Figure 40. Effect of H₂S on methane reforming performance over NiAl₂O₄ (LT) catalyst under the conditions of 850°C, 20 ppm H₂S, 29.3% CH₄, 58.1%CO₂, 12.6% N₂ and GHSV = 60,000 hr⁻¹.

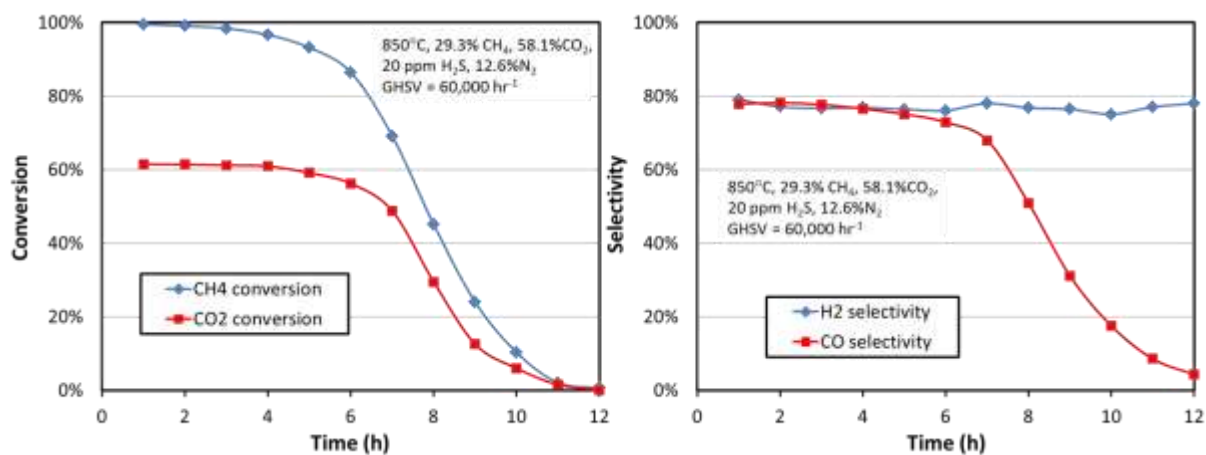


Figure 41. Effect of H₂S on methane reforming performance over NiAl₂O₄ catalyst under the conditions of 850°C, 20 ppm H₂S, 29.3% CH₄, 58.1%CO₂, 12.6% N₂ and GHSV = 60,000 hr⁻¹.

Equation 1. Equations used to calculate conversions, yields, and selectivities in the above figures.

$$\text{Reactant Conversion} = 100 \times \frac{(\text{Moles of X Converted})}{(\text{Moles of X in Feed})}$$

$$\text{Product Yield for H}_2 = 100 \times \frac{(2 \times \text{Moles of X Converted})}{(\text{Moles of H in Feed})}$$

$$\text{Product Selectivity for CO} = 100 \times \frac{(\text{Moles of CO produced})}{(\text{Moles of CO} + \text{CO}_2)}$$

$$\text{Product Selectivity for H}_2 = 100 \times \left[\frac{\left(\frac{(2 \times \text{Moles of H}_2 \text{ Produced})}{(\text{Total Moles of H in Feed})} \right)}{\text{CH}_4 \text{ Conversion}} \right]$$

Previous studies have indicated that the presence of Co has a beneficial effect because it can oxidize soot, but it can also oxidize more easily than Ni.¹⁰² The Ni and Co, when present as a bimetallic, can work together to allow high catalytic activity while preventing deactivation, although the exact mechanism causing this is unknown.¹⁰² Excess Co present in a bimetallic slows deactivation, while monometallic Co catalysts have low activity due to its tendency to oxidize.¹⁰⁷

The change in microstructure of the defect spinel as calcination temperature increases may have an effect on its catalytic activity. SEM images shown in Fig. 42 show the morphology of the samples after catalytic activity testing. The more faceted sample (left) had a lower catalytic activity than the less faceted sample (right).

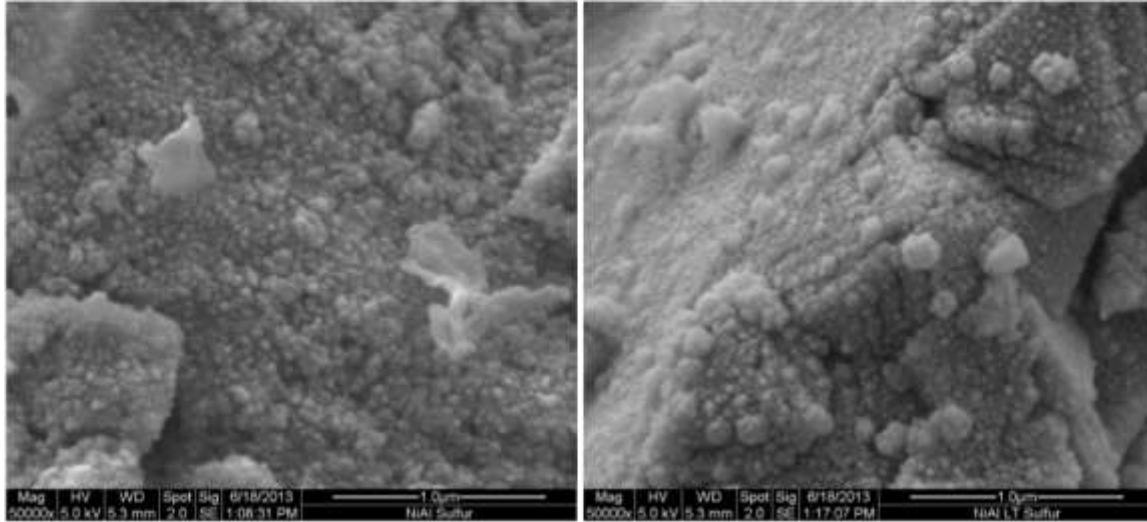


Figure 42. Post-situ SEM images of NiAl_2O_4 samples sent for catalytic activity testing. The image on the left shows a less faceted defect spinel calcined at 1300°C 36hrs. and the image on the right shows a more faceted defect spinel calcined at 1500°C 8hrs.

5. Exposure to Methane

Powders were both reduced in methane and exposed to methane after being reduced in flowing hydrogen. In both cases, carbon filaments grew as a result of methane decomposition, lifting the catalytic metal off the surface of the spinel. Evidence of this can be seen in Figures 43-44. The metal particles remain at the tip of the filaments after exposure. There is a variation in diameter of the filaments caused by corresponding variation in metal particle size.

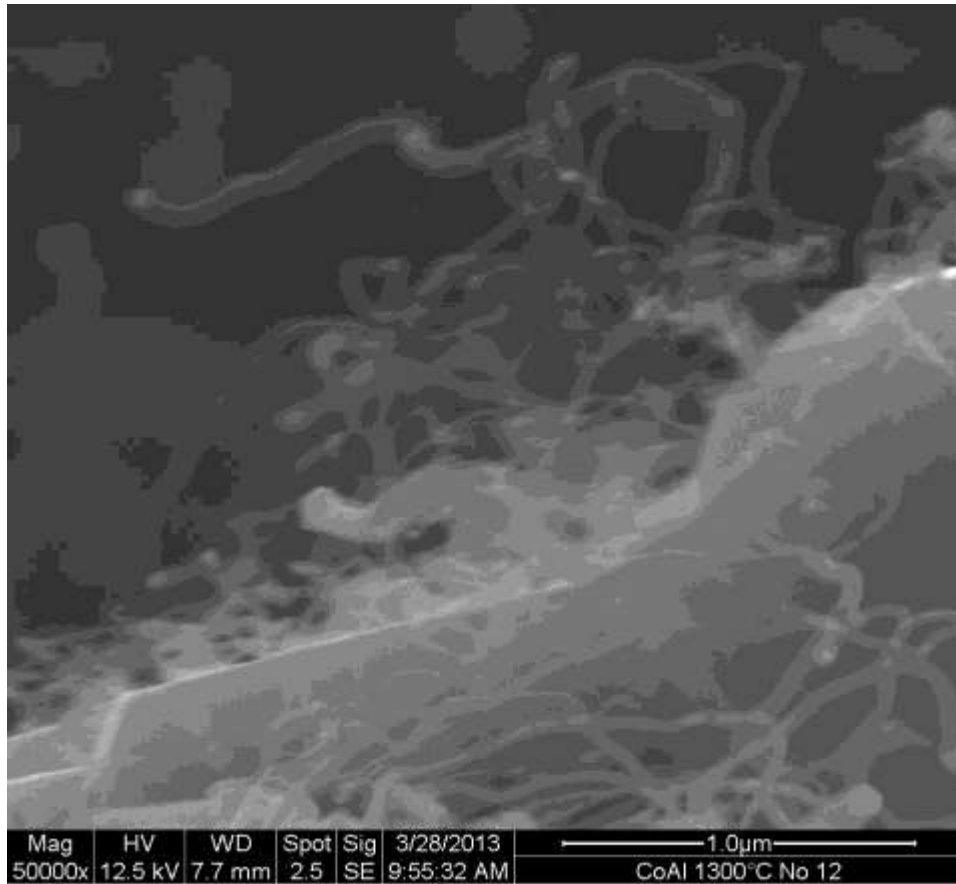


Figure 43. CoAl_2O_4 calcined at 1300°C for 36 hours and reduced in methane at 850°C for 8 hours. Metallic Co particle can be seen atop a carbon filament in the upper left.

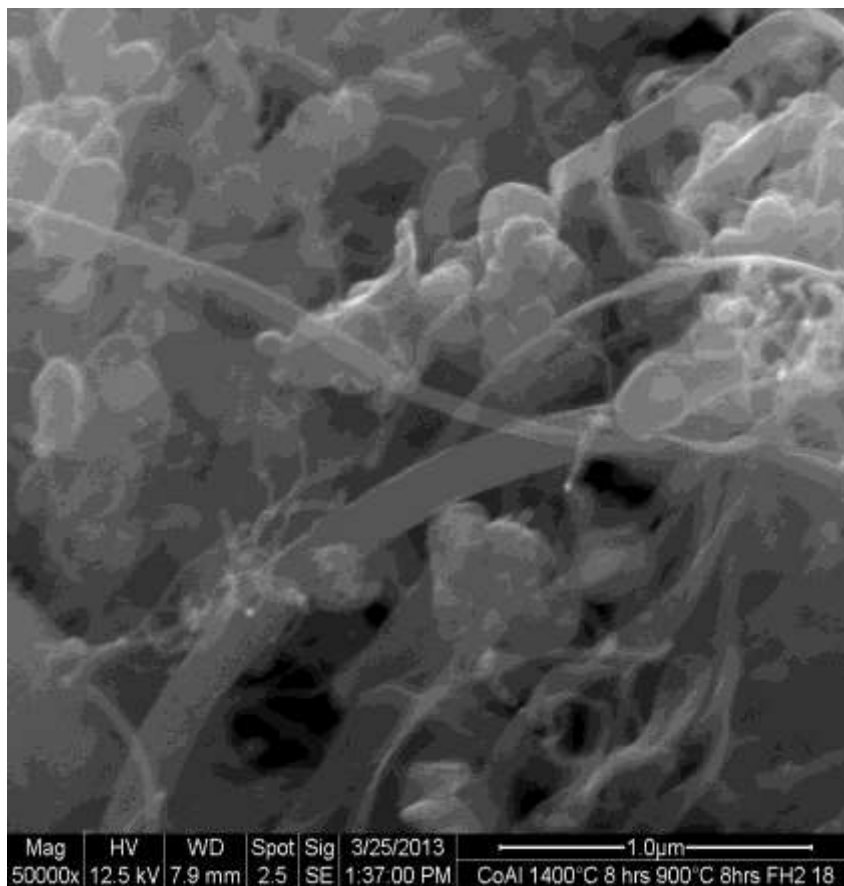


Figure 44. CoAl_2O_4 calcined at 1400°C for 8 hours, reduced in flowing H_2 at 900°C for 8 hours, and exposed to methane at 800°C for 3 hours. Variations in size of the carbon filaments can be seen, which are caused by variations in size of metal particles.

To investigate the behavior of the lifted metal upon removal of carbon, the samples were heated to 350°C in air with a dwell of 8 hours, followed by more SEM studies. Figures 45-46 show that the Ni metal particles are not in the same ordered fashion along the facets as they were when they formed during initial reduction. This is likely due to the fact that the carbon filaments lifted the metal particles off the surface and dropped them in a different area upon burning.

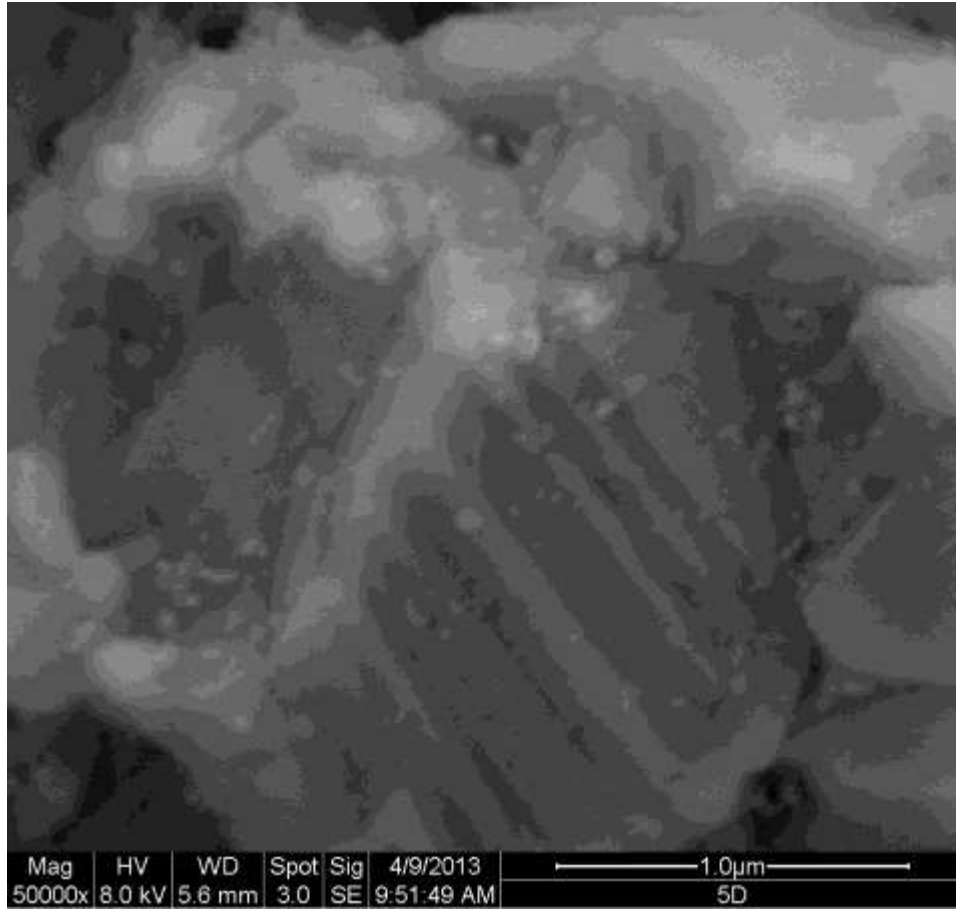


Figure 45. $\text{Ni}_{0.5}\text{Co}_{0.5}\text{Al}_2\text{O}_4$ calcined at 1500°C for 8 hours, reduced in CH_4 for 8 hours, then exposed to air at 350°C to remove carbon without reoxidizing.

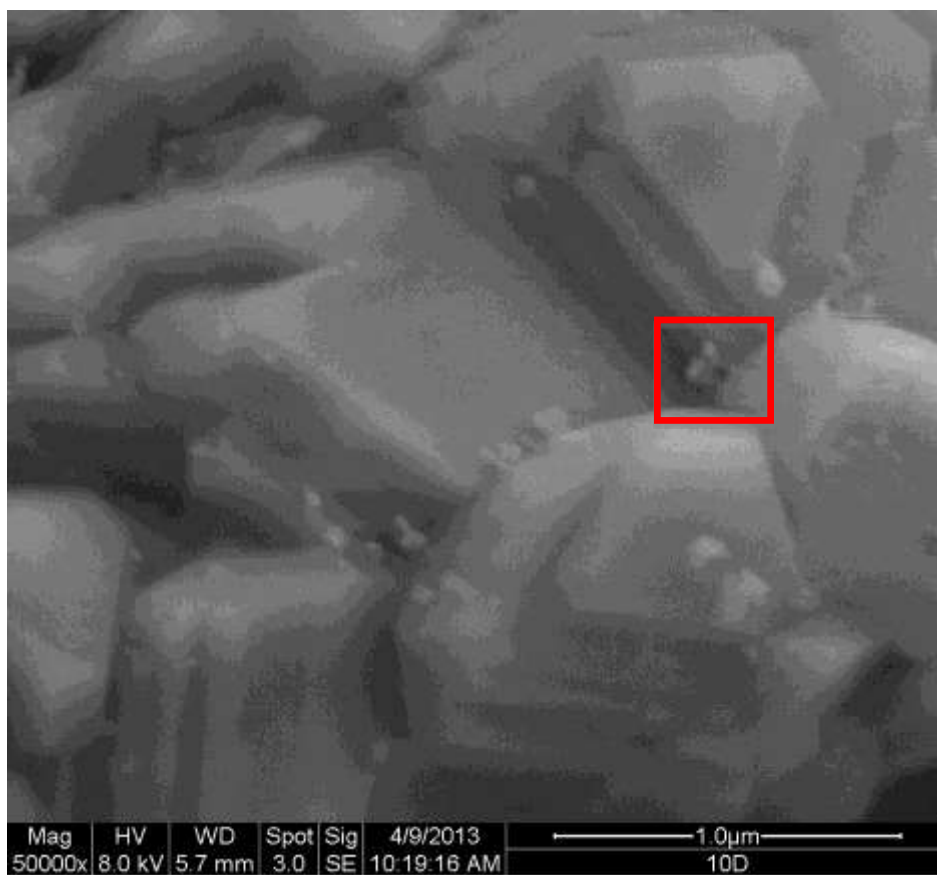


Figure 46. NiAl₂O₄ calcined at 1300°C for 36 hours and reduced in CH₄ for 8 hours, then exposed to air at 350°C to remove carbon buildup. Very short carbon filaments can be seen (highlighted) with small Ni metal particles on top of them.

D. Summary and Conclusions

The aluminate spinels are cost effective and highly catalytic alternative to expensive precious metals as catalysts. Their ability to regenerate is useful in the case of fuel cell anodes which acquire carbon buildup and subsequently lose catalytic ability in hydrocarbon fuels. The microstructure of the spinels can be tailored by altering the calcination and reduction temperatures. The reoxidation and re-reduction cycle can be used to produce a clean, catalytic defect spinel supported Ni or Co catalyst without degradation of the structure through several cycles.

E. Future Work

Future studies should focus on the reason behind the high catalytic activity of the material considering the relatively low surface area of catalytic metal. The exact growth mechanism of

the metallic nanoparticles resulting in the highly faceted morphology also needs to be mapped out.

III. EFFECT OF SPINEL ADDITIONS ON NI/YSZ CELL PERFORMANCE IN HYDROCARBON FUELS

A. Experimental Procedure

1. Cell Preparation

Electrolyte-supported cells were made using commercial 20mm diameter 300-350 micron thick YSZ disks (Fuel Cell Materials). Anode consisted of NiO (97%, Fisher Scientific) and yttria stabilized zirconia (99%, Fisher Scientific) mixed in a 1:1 mass ratio and placed in a vibratory mill for 1 hour in isopropanol. The powder was then mixed with ink vehicle at 30 weight percent solids and painted on one side of the electrolyte disk. The anode was dried for 1 hour at 500°C and sintered at 1500°C for 8 hours in the same furnace. After cooling, LSM-YSZ composite cathode paste (50 wt. % $(La_{0.80}Sr_{0.20})_{0.95}MnO_{3-x}$ and 50wt. % $(Y_2O_3)_{0.08}(ZrO_2)_{0.92}$, Fuel Cell Materials) was painted on the other side and sintered at 1000°C for 8 hours. To add the 10 and 20 volume percentages of spinel, a small amount of spinel was mixed with isopropanol in an alumina mortar and pestle and wet impregnated into the porous anode, then dried.

2. Fuel Cell Testing Setup

Power density measurements were collected using the NexTech Probostat button cell test apparatus (Fig. 47). The button cell was placed on top of an inner alumina tube, using a glass sealant material to form a viscous seal between the cell and the inner tube. Electrode leads were placed in contact with the anode (from the bottom) and cathode (from the top). A spring-loaded plate placed on top of the cathode current collector and affixed to the bottom of the inner tube was used to apply pressure on the cell. The pressure keeps both current collectors in contact with the electrodes. A second outer alumina tube is placed over the assembly, forming 2 gas volumes separated by the cell. The assembly was placed inside a vertically mounted tube furnace. The system was heated at 10°C/minute to 850°C and held for the duration of the experiment. The inner gas volume, in contact with the anode, was fed with a 4% H_2/N_2 gas mix or humidified or dry methane. The outer gas volume, in contact with the cathode, was fed with breathing quality

air. The seal was checked for leakage prior to starting the turning on the fuel gas.

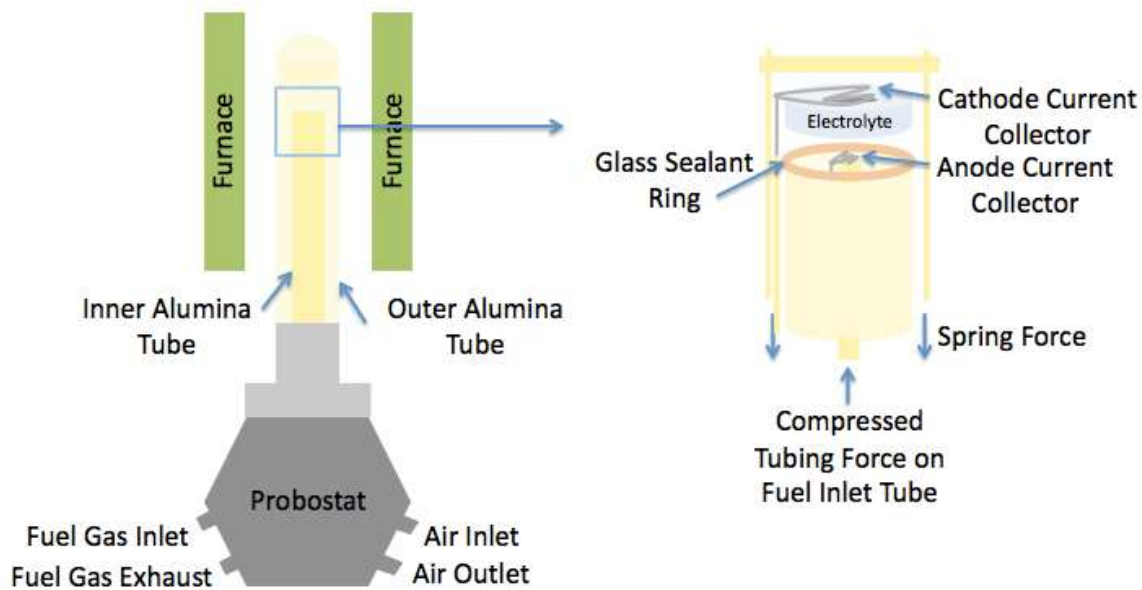


Figure 47. Schematic showing Probostat within furnace and a cross-section showing the cell placement inside the outer alumina tube.

3. Characterization

a. Power Density Measurements

The BK Precision 300W Programmable DC Electronic Load Model 8500 was used in constant voltage mode between 1.1 and 0.1V in steps of 0.1V. Current and power were measured at each step. SEM micrographs were collected before and after testing as a cross section and on the anode surface.

b. Standard Voltage Scanned Electron Microscopy

An FEI Quanta 200F Environmental Scanning Electron Microscope was used to collect all standard voltage electron micrographs. Samples were dispersed onto carbon planchets and carbon coated, unless they were considerably coated by carbon filaments already.

B. Results and Discussion

1. Cell Performance

a. Cell Structure

Cross-sections of CoAl_2O_4 and NiAl_2O_4 anodes printed on a commercial YSZ substrate can be seen in Figure 48. In both cases, small metallic particles can be seen on the surface of a

porous support structure. This porosity is advantageous because it allows the fuel to infiltrate the anode, creating more active sites for catalysis.

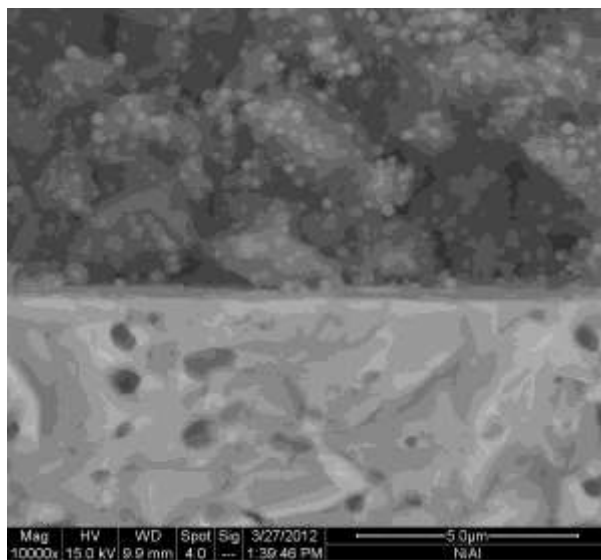


Figure 48. SEM image of cross-section of YSZ electrolyte coated with $\text{NiAl}_2\text{O}_4/\text{NiO}/\text{YSZ}$ composite anode.

Porosity and gas permeability are critical properties in SOFC anode morphology. They are typically characterized using SEM imaging, although some BET systems can effectively find surface area, which will be higher in porous structures. A specific surface area of catalyst will provide more active sites for catalysis to take place, resulting in more hydrocarbon fuel being converted to H_2 at the anode. It will also lead to more carbon formation (coking) on the surface as metal catalysts catalyze carbon nanotube formation. As seen in Figure 46, porosity is present in the spinel samples printed on the YSZ electrolyte.

b. Effect of Spinel Additions

Using 4% H_2 in N_2 as fuel, NiAl_2O_4 has a peak power density comparable to traditional Ni/YSZ. (Fig. 49) The peak powder density decreases with increasing Co content. Using methane, all three of the samples with spinel additions had considerably lower peak power density than the standard Ni/YSZ cell. (Fig. 50) Voltage curves show a similar trend to the power density curves. (Fig. 51)

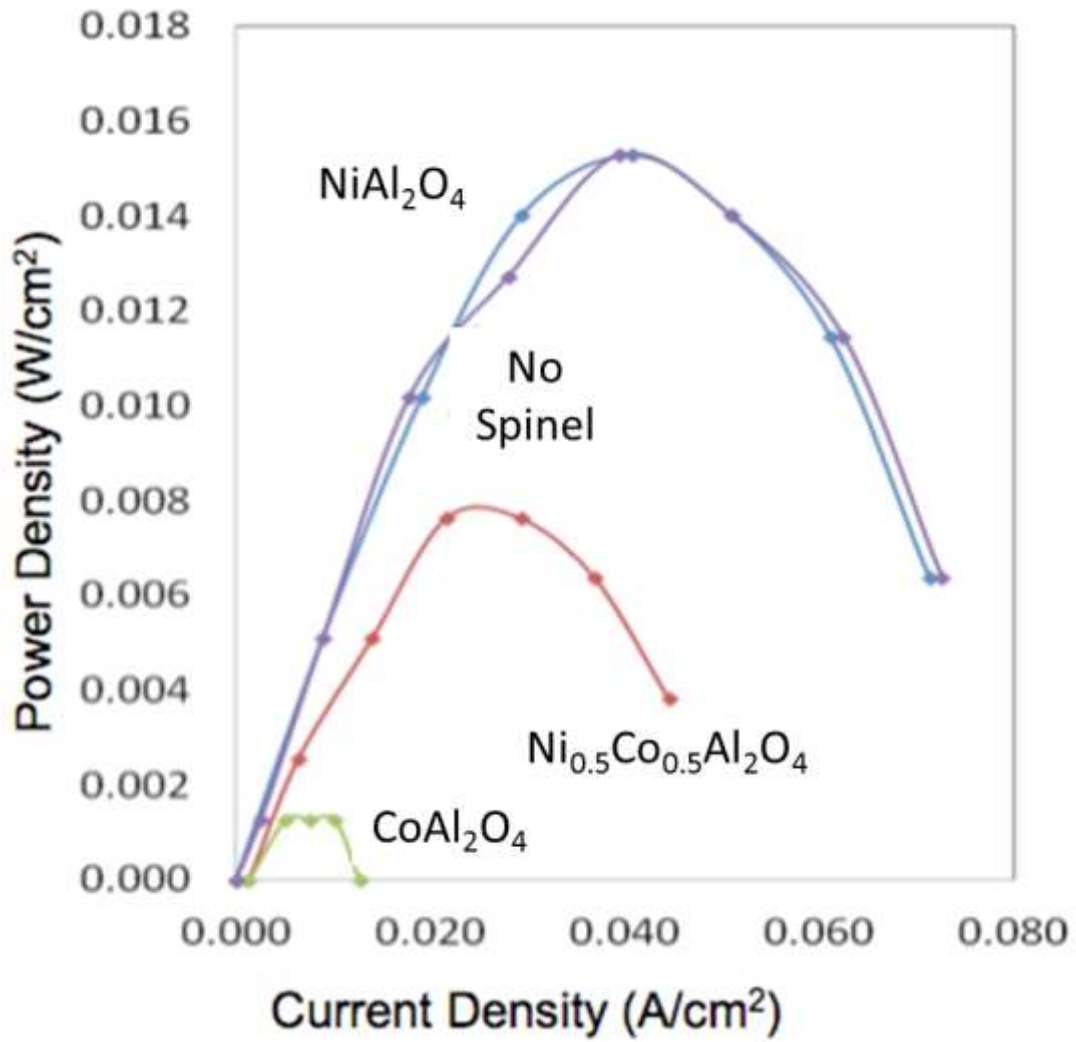


Figure 49. Power density using hydrogen fuel of cells containing 3 different spinels in the anode vs. a traditional NiO/YSZ anode.

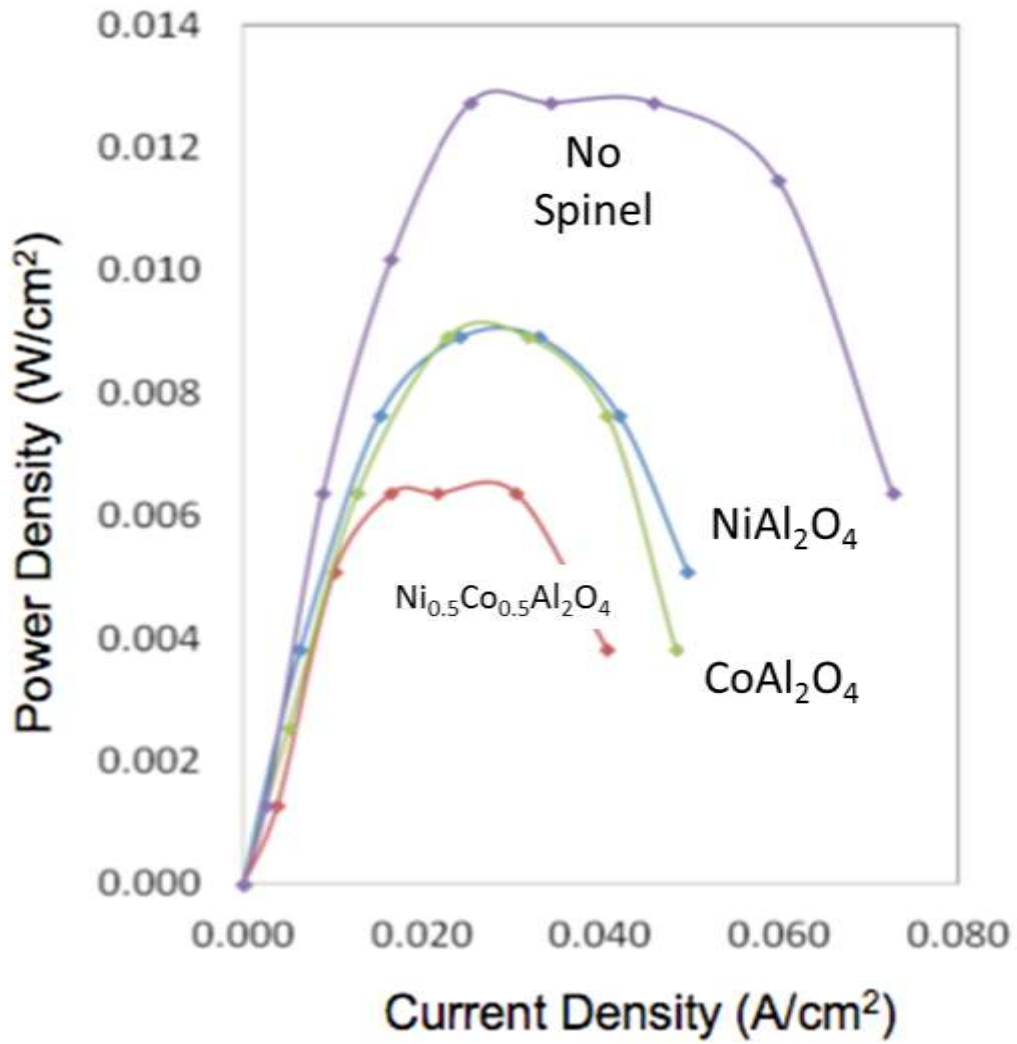


Figure 50. Power density using methane fuel of 3 different spinel compositions included in the anode, shown vs. a traditional NiO/YSZ anode.

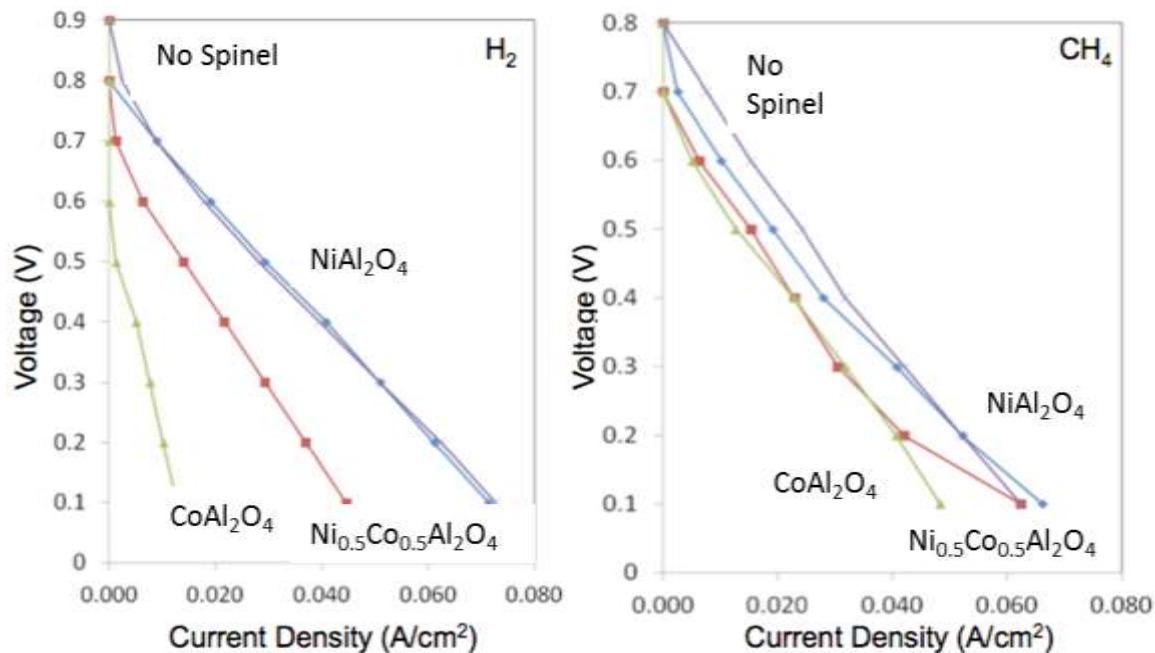


Figure 51. Voltage curves for samples containing 3 different spinel compositions vs. traditional NiO/YSZ anode.

C. Future Work

The fabrication process for the SOFC button cells needs to be optimized to reduce anode cracking upon sintering. Low power density measurements can be the result of high internal resistance within the cell, which can be reduced by increasing NiO content.

D. Summary and Conclusions

The defect spinel supported nanoparticulate catalysts exhibit high catalytic activity even though specific surface area as measured by H₂ adsorption is lower than for standard catalyst. The morphology of the catalyst is very faceted at high calcination and reduction temperatures. Corners and edges typically have more catalytic sites present, which means that the faceting could be beneficial. No phase changes occur with reoxidation-reduction cycles, which is critical for repeated cycling in an anode.

REFERENCES

1. E. Fabbri, D. Pergolesi, and E. Traversa, "Electrode Materials: A Challenge for the Exploitation of Protonic Solid Oxide Fuel Cells," *Sci. Technol. Adv. Mater.*, **11** [4] 1-9 (2010).
2. J. Rostrup-Nielsen, "Reaction Kinetics and Scale-up of Catalytic Processes," *J. Mol. Catal. A: Chem.*, **163** [1-2] 157-62 (2000).
3. C. Song, "Fuel Processing for Low-Temperature and High-Temperature Fuel Cells. Challenges, and Opportunities for Sustainable Development in the Twenty-First Century," *Catal. Today*, **77** [1-2] 17-49 (2002).
4. A.C.S.C. Teixeira and R. Giudici, "A Monte Carlo Model for the Sintering of Ni/Al₂O₃ Catalysts," *Chem. Eng. Sci.*, **56** [3] 789-98 (2001).
5. A.C.S.C. Teixeira and R. Giudici, "Sintering of Metal Crystallites in Ni/Al₂O₃ Catalysts Used for Steam Reforming: An Experimental Design Study," *Stud. Surf. Sci. Catal.*, **139** [1] 495-502 (2001).
6. S.Q. Chen and Y. Liu, "LaFeYNi_{1-y}O₃ Supported Nickel Catalysts Used for Steam Reforming of Ethanol," *Int. J. Hydrogen Energy*, **34** [21] 4735-46 (2009).
7. W. Niemann, H.J.H. Bak, B.S. Clausen, B. Fastrup, B. Fabius, J. Villadsen, T. Wroblewski, and H. Topsoe, "High Resolution Powder XRD Studies of Steam Reforming Catalysts," *Conf. Proc. - Ital. Phys. Soc.*, **25** [1] 575-8 (1990).
8. S. Takenaka, Y. Orita, H. Umabayashi, H. Matsune, and M. Kishida, "High Resistance to Carbon Deposition of Silica-Coated Ni Catalysts in Propane Steam Reforming," *Appl. Catal., A*, **351** [2] 189-94 (2008).
9. L. Zhou, Y. Guo, Q. Zhang, M. Yagi, H. Li, J. Chen, M. Sakurai, and H. Kameyama, "Self-Activation and Self-Regenerative Activity of Trace Ru-Doped Plate-Type Anodic Alumina Supported Nickel Catalysts in Steam Reforming of Methane," *Catal. Commun.*, **10** [3] 325-9 (2008).
10. Q. Geng, X. Huang, Q. Huang, and W. Li, "Studies on the Sulfur Dioxide Resistance of Cobalt-Containing Perovskite-Type Oxidation Catalysts," *Cuihua Xuebao*, **10** [1] 79-82 (1989).
11. Q. Huang, N. Wu, Q. Chen, and W. Li, "Catalytic Properties and Sulfur Dioxide Resistance of Manganese-Based Perovskite-Type Oxides," *Beijing Gongye Daxue Xuebao*, **18** [1] 83-8 (1992).
12. D. Jovanovic, V. Dondur, A. Terlecki-Baricevic, and B. Grbic, "Three-Way Activity and

- Sulfur Tolerance of Single Phase Perovskites," *Stud. Surf. Sci. Catal.*, **71** [1-2] 371-9 (1991).
13. W. Li, H. Dai, and Y. Lieu, "Improving Sulfur Dioxide Resistance of Base Metal Perovskite Type Oxidation Catalyst," *Stud. Surf. Sci. Catal.*, **75** [1-2] 1793-6 (1993).
 14. T. Yoshizumi, C. Uryu, T. Oshima, Y. Shiratori, K. Ito, and K. Sasaki, "Sulfur Poisoning of SOFCs: Dependence on Operational Parameters," *ECS Trans.*, **35** [1] 1717-25 (2011).
 15. S. Wang, M. Liu, and J. Winnick, "Stabilities and Electrical Conductivities of Electrode Materials for Use in H₂S-Containing Gases," *J. Solid State Electrochem.*, **5** [3] 188-95 (2001).
 16. C. Yates and J. Winnick, "Anode Materials for a Hydrogen Sulfide Solid Oxide Fuel Cell," *J. Electrochem. Soc.*, **146** [8] 2841-4 (1999).
 17. C. Song, "Fuel Processing for Low-Temperature and High-Temperature Fuel Cells: Challenges, and Opportunities for Sustainable Development in the 21st Century," *Catal. Today*, **77** [1-2] 17-49 (2002).
 18. G.J. Offer, J. Mermelstein, E. Brightman, and N.P. Brandon, "Thermodynamics and Kinetics of the Interaction of Carbon and Sulfur with Solid Oxide Fuel Cell Anodes," *J. Am. Ceram. Soc.*, **92** [4] 763-80 (2009).
 19. Q. Xu, M. Zhou, P. Lan, Z. Ren, S. Zhang, and Y. Yan, "Deactivation and Regeneration of Catalyst for Steam Reforming of Bio-Oil to Produce Hydrogen," *Shiyou Huagong*, **39** [1] 849-54 (2010).
 20. T.N. Serezhina, Y.I. Melnik, O.V. Nevzorova, and I.N. Karyazma, "Reduction of Copper Manganite by Hydrogen," *Izv. Akad. Nauk SSSR, Met.*, 1 [1] 27-9 (1990).
 21. A.A. Khasin, T.M. Yur'eva, L.M. Plyasova, G.N. Kustova, H. Jovic, A. Ivanov, Y.A. Chesalov, V.I. Zaikovskii, A.V. Khasin, L.P. Davydova, and V.N. Parmon, "Mechanistic Features of Reduction of Copper Chromite and State of Absorbed Hydrogen in the Structure of Reduced Copper Chromite," *Russ. J. Gen. Chem.*, **78** [11] 2203-13 (2008).
 22. S.H. Lim, S. Desu, and A.C. Rastogi, "Chemical Spray Pyrolysis Deposition and Characterization of P-Type CuCr_{1-x}Mg_xO₂ Transparent Oxide Semiconductor Thin Films," *J. Phys. Chem. Solids*, **69** [8] 2047-56 (2008).
 23. K. Faungnawakij, N. Shimoda, T. Fukunaga, R. Kikuchi, and K. Eguchi, "Crystal Structure and Surface Species of CuFe₂O₄ Spinel Catalysts in Steam Reforming of Dimethyl Ether," *Appl. Catal., B*, **92** [3-4] 341-50 (2009).
 24. E. Uestuendag, Z. Zhang, M.L. Stocker, P. Rangaswamy, M.A.M. Bourke, S. Subramanian, K.E. Sickafus, J.A. Roberts, and S.L. Sass, "Influence of Residual Stresses

- on the Evolution of Microstructure During the Partial Reduction of NiAl_2O_4 ," *Mater. Sci. Eng., A*, **A238** [1] 50-65 (1997).
25. H. Muroyama, R. Nakase, T. Matsui, and K. Eguchi, "Ethanol Steam Reforming over Ni-Based Spinel Oxide," *Int. J. Hydrogen Energy*, **35** [4] 1575-81 (2010).
 26. H. Tanaka and Y. Nishihata, "Self-Regenerative Function of the Intelligent Automotive Catalyst," *Kino Zairyo*, **27** [7] 61-70 (2007).
 27. H. Tanaka, "An Intelligent Catalyst: The Self-Regenerative Palladium-Perovskite Catalyst for Automotive Emissions Control," *Catalysis Surveys from Asia*, **9** [2] 63-74 (2005).
 28. A. Orera and P.R. Slater, "New Chemical Systems for Solid Oxide Fuel Cells," *Chem. Mater.*, **22** [3] 675-90 (2010).
 29. S. Tao and J.T.S. Irvine, "Discovery and Characterization of Novel Oxide Anodes for Solid Oxide Fuel Cells," *Chem. Rec.*, **4** [2] 83-95 (2004).
 30. Z. Cheng, J.H. Wang, and M. Liu, "Anodes"; pp.73-130 in Solid Oxide Fuel Cells: Materials Properties and Performance, Vol. 1, *Green Chemistry and Chemical Engineering*. Edited by J. Fergus. CRC Press, Boca Raton, FL, 2008.
 31. Z. Cheng, J.-H. Wang, Y. Choi, L. Yang, M.C. Lin, and M. Liu, "From Ni-YSZ to Sulfur-Tolerant Anode Materials for SOFCs: Electrochemical Behavior, In-Situ Characterization, Modeling, and Future Perspectives," *Energy Environ. Sci.*, **4** [4] 4380-409 (2011).
 32. Z. Cheng, S. Zha, and M. Liu, "Stability of Materials as Candidates for Sulfur-Resistant Anodes of Solid Oxide Fuel Cells," *J. Electrochem. Soc.*, **153** [7] A1302-A9 (2006).
 33. S. Choi, J. Wang, Z. Cheng, and M. Liu, "Surface Modification of Ni-YSZ Using Niobium Oxide for Sulfur-Tolerant Anodes in Solid Oxide Fuel Cells," *J. Electrochem. Soc.*, **155** [5] B449-B54 (2008).
 34. Z. Cheng, S. Zha, L. Aguilar, and M. Liu, "Chemical, Electrical, and Thermal Properties of Strontium Doped Lanthanum Vanadate," *Solid State Ionics*, **176** [1] 1921-8 (2005).
 35. L. Aguilar, S. Zha, Z. Cheng, J. Winnick, and M. Liu, "A Solid Oxide Fuel Cell Operating on Hydrogen Sulfide (H_2S) and Sulfur-Containing Fuels," *J. Power Sources*, **135** [1-2] 17-24 (2004).
 36. L. Aguilar, S. Zha, S. Li, J. Winnick, and M. Liu, "Sulfur-Tolerant Materials for the Hydrogen Sulfide SOFC," *Electrochem. Solid-State Lett.*, **7** [1] A324-A6 (2004).
 37. M.K. Bruce, M.V.D. Bossche, and S. McIntosh, "The Influence of Current Density on the

- Electrocatalytic Activity of Oxide-Based Direct Hydrocarbon SOFC Anodes," *J. Electrochem. Soc.*, **155** [11] B1202-B9 (2008).
38. B. Huang, X.J. Zhu, W.Q. Hu, Y.Y. Wang, and Q.C. Yu, "Characterization of the Ni-Scsz Anode with a LSCM-CeO₂ Catalyst Layer in Thin Film Solid Oxide Fuel Cell Running on Ethanol Fuel," *J. Power Sources*, **195** [10] 3053-9 (2010).
 39. Y. Zheng, W. Zhou, R. Ran, and Z. Shao, "Perovskite as Anode Materials for Solid Oxide Fuel Cells," *Huaxue Jinzhan*, **20** [1] 413-21 (2008).
 40. A.L. Dicks, "Advances in Catalysts for Internal Reforming in High Temperature Fuel Cells," *J. Power Sources*, **71** [1-2] 111-22 (1998).
 41. J.W. Fergus, "Oxide Anode Materials for Solid Oxide Fuel Cells," *Solid State Ionics*, **177** [17-18] 1529-41 (2006).
 42. R.J. Gorte, J.M. Vohs, and S. McIntosh, "Recent Developments on Anodes for Direct Fuel Utilization in SOFC," *Solid State Ionics*, **175** [1-4] 1-6 (2004).
 43. M. Mogensen, K.V. Jensen, M.J. Jorgensen, and S. Primdahl, "Progress in Understanding SOFC Electrodes," *Solid State Ionics*, **150** [1-2] 123-9 (2002).
 44. A. Civera, M. Pavese, G. Saracco, and V. Specchia, "Combustion Synthesis of Perovskite-Type Catalysts for Natural Gas Combustion," *Catal. Today*, **83** [1-4] 199-211 (2003).
 45. S. Zha, P. Tsang, Z. Cheng, and M. Liu, "Electrical Properties and Sulfur Tolerance of La_{0.75}Sr_{0.25}Cr_{1-x}Mn_xO₃ under Anodic Conditions," *J. Solid State Chem.*, **178** [6] 1844-50 (2005).
 46. Z. Cheng, S. Zha, L. Aguilar, D. Wang, J. Winnick, and M. Liu, "A Solid Oxide Fuel Cell Running on H₂S/CH₄ Fuel Mixtures," *Electrochem. and Solid-State Lett.*, **9** [1] A31-A3 (2006).
 47. J.M. Haag, S.A. Barnett, J.W. Richardson, and K.R. Poepelmeier, "Structural and Chemical Evolution of the SOFC Anode La_{0.30}Sr_{0.70}Fe_{0.70}Cr_{0.30}O₃ Upon Reduction and Oxidation: An In-Situ Neutron Diffraction Study," *Chem. Mater.*, **22** [10] 3283-9 (2010).
 48. Z. Cheng, S. Zha, and M. Liu, "Stability of Materials as Candidates for Sulfur-Resistant Anodes of Solid Oxide Fuel Cells," *J. Electrochem. Soc.*, **153** [7] A1302-A9 (2006).
 49. X.J. Chen, Q.L. Liu, S.H. Chan, N.P. Brandon, and K.A. Khor, "Sulfur Tolerance and Hydrocarbon Stability of La_{0.75}Sr_{0.25}Cr_{0.5}Mn_{0.5}O₃/Gd_{0.2}Ce_{0.8}O_{1.9} Composite Anode under Anodic Polarization," *J. Electrochem. Soc.*, **154** [11] B1206-B10 (2007).
 50. M. Mogensen and P. Holtappels, "Ni-Based Solid Oxide Cell Electrodes" pp. 25-38 in

Solid Oxide Fuel Cells: Facts and Figures. Edited by J. Irvine. Springer, London, U.K.. (2013)

51. S. Li, W. Rauch, M. Liu, A. Burke, and J. Winnick, "New Sulfur-Tolerant Electrode Materials for H₂S Removal and Sofcs," *Proc. - Electrochem. Soc.*, **2002-26** [1] 113-21 (2003).
52. O.A. Marina, N.L. Canfield, and J.W. Stevenson, "Thermal, Electrical, and Electrocatalytical Properties of Lanthanum-Doped Strontium Titanate," *Solid State Ionics*, **149** [1-2] 21-8 (2002).
53. D.P. Fagg, V.V. Kharton, A.V. Kovalevsky, A.P. Viskup, E.N. Naumovich, and J.R. Frade, "The Stability and Mixed Conductivity in La and Fe Doped SrTiO₃ in the Search for Potential SOFC Anode Materials," *J. Eur. Ceram. Soc.*, **21** [10-11] 1831-5 (2001).
54. P.R. Slater, D.P. Fagg, and J.T.S. Irvine, "Synthesis and Electrical Characterization of Doped Perovskite Titanates as Potential Anode Materials for Solid Oxide Fuel Cells," *J. Mater. Chem.*, **7** [1] 2495-8 (1997).
55. Tao and J.T.S. Irvine, "Catalytic Properties of the Perovskite Oxide La_{0.75}Sr_{0.25}Cr_{0.5}Fe_{0.5}O_{3-x} in Relation to Its Potential as a Solid Oxide Fuel Cell Anode Material," *Chem. Mater.*, **16** [21] 4116-21 (2004).
56. S. Tao and J.T.S. Irvine, "A Redox-Stable Efficient Anode for Solid-Oxide Fuel Cells," *Nat. Mater.*, **2** [5] 320-3 (2003).
57. S. Tao and J.T.S. Irvine, "Synthesis and Characterization of La_{0.75}Sr_{0.25}Cr_{0.5}Mn_{0.5}O_{3-δ}, a Redox-Stable, Efficient Perovskite Anode for SOFCs," *J. Electrochem. Soc.*, **151** [2] A252-A9 (2004).
58. S. Tao and J.T.S. Irvine, "Phase Transition in Perovskite Oxide La_{0.75}Sr_{0.25}Cr_{0.5}Mn_{0.5}O_{3-δ} Observed by in Situ High-Temperature Neutron Powder Diffraction," *Chemistry of Materials*, **18** [23] 5453-60 (2006).
59. Tao, J.T.S. Irvine, and S.M. Plint, "Methane Oxidation at Redox Stable Fuel Cell Electrode La_{0.75}Sr_{0.25}Cr_{0.5}Mn_{0.5}O_{3-δ}," *J. Phys. Chem. B*, **110** [43] 21771-6 (2006).
60. Q.X. Fu, F. Tietz, and D. Stover, "La_{0.4}Sr_{0.6}Ti_{1-x}Mn_xO_{3-δ} Perovskites as Anode Materials for Solid Oxide Fuel Cells," *J. Electrochem. Soc.*, **153** [4] D74-D83 (2006).
61. M.A. Buccheri and J.M. Hill, "Gas Product Analysis During the Electrochemical Conversion of Dry Methane with a La_{0.3}Sr_{0.7}TiO₃ and Ni/YSZ Bi-Layer SOFC Anode," *ECS Trans.*, **35** [1] 1551-61 (2011).
62. P. Vernoux, E. Djurado, and M. Guillodo, "Catalytic and Electrochemical Properties of Doped Lanthanum Chromites as New Anode Materials for Solid Oxide Fuel Cells," *J.*

- Am. Ceram. Soc.*, **84** [10] 2289-95 (2001).
63. K. Kourtakis, A.M. Gaffney, and L. Wang, Conoco Inc., "Chromium-Based Non-Perovskite Coke-Resistant Catalysts for Partial Oxidation of Hydrocarbons to Synthesis Gas," Pat. 2001.
 64. P.H. Larsen, C. Chung, and M. Mogensen, Risoe National Laboratory, "Solid Oxide Fuel Cell with Redox-Stable Anode," Pat. 2006.
 65. M.A. Buccheri, A. Singh, and J.M. Hill, "Anode- Versus Electrolyte-Supported Ni-YSZ/YSZ/Pt SOFCs: Effect of Cell Design on OCV, Performance and Carbon Formation for the Direct Utilization of Dry Methane," *J. Power Sources*, **196** [3] 968-76 (2011).
 66. M. Cimenti and J.M. Hill, "Direct Utilization of Liquid Fuels in SOFC for Portable Applications: Challenges for the Selection of Alternative Anodes," *Energies (Basel, Switz.)*, **2** [2] 377-410 (2009).
 67. S. Islam, "Preparation of Carbon-Tolerant Solid Oxide Fuel Cell Anodes for Direct Utilization of CH₄ using Microwave Irradiation"; Ph.D. Thesis. University of Calgary, Calgary, Alberta, 2013.
 68. S. Islam and J. Hill, "Barium oxide promoted Ni/YSZ solid-oxide fuel cells for direct utilization of methane," *J. Mater. Chem. A*, **2** [1] 1922-1929 (2014)
 69. K. Nikooyeh, R. Clemmer, V. Alzate-Restrepo, and J.M. Hill, "Effect of Hydrogen on Carbon Formation on Ni/YSZ Composites Exposed to Methane," *Appl. Catal., A*, **347** [1] 106-11 (2008).
 70. S. Islam and J.M. Hill, "Microwave-Assisted Preparation of Cu Coated Ni/YSZ Anode for Direct Utilization of Dry CH₄ in Sofc," *ECS Trans.*, **35** [1] 1389-95 (2011).
 71. S. Islam and J.M. Hill, "Preparation of Cu-Ni/YSZ Solid Oxide Fuel Cell Anodes Using Microwave Irradiation," *J. Power Sources*, **196** [11] 5091-4 (2011).
 72. M. Cimenti and J.M. Hill, "Direct Utilization of Methanol and Ethanol in Solid Oxide Fuel Cells Using Cu-Co(Ru)/Zr_{0.35}Ce_{0.65}O_{2-δ} Anodes," *J. Power Sources*, **195** [13] 3996-4001 (2010).
 73. S.M. Hashemnejad and M. Parvari, "Deactivation and Regeneration of Nickel-Based Catalysts for Steam-Methane Reforming," *Cuihua Xuebao*, **32** [1] 273-9 (2011).
 74. A.M. Karim, Y. Su, J. Sun, C. Yang, J.J. Strohm, D.L. King, and Y. Wang, "A Comparative Study between Co and Rh for Steam Reforming of Ethanol," *Appl. Catal., B*, **96** [3-4] 441-8 (2010).
 75. D. Li, T. Shishido, Y. Oumi, T. Sano, and K. Takehira, "Self-Activation and Self-

- Regenerative Activity of Trace Rh-Doped Ni/Mg(Al)O Catalysts in Steam Reforming of Methane," *Appl. Catal., A*, **332** [1] 98-109 (2007).
76. E.B. Pereira, N. Homs, S. Marti, J.L.G. Fierro, and d.I.P.P. Ramirez, "Oxidative Steam-Reforming of Ethanol over Co/SiO₂, Co-Rh/SiO₂ and Co-Ru/SiO₂ Catalysts: Catalytic Behavior and Deactivation/Regeneration Processes," *J. Catal.*, **257** [1] 206-14 (2008).
 77. L. Zhou, Y. Guo, Q. Zhang, M. Yagi, H. Li, J. Chen, M. Sakurai, and H. Kameyama, "Self-Activation and Self-Regenerative Activity of Trace Ru-Doped Plate-Type Anodic Alumina Supported Nickel Catalysts in Steam Reforming of Methane," *Catal. Commun.*, **10** [3] 325-9 (2008).
 78. N. Shimoda, H. Muroyama, T. Matsui, K. Faungnawakij, R. Kikuchi, and K. Eguchi, "Dimethyl Ether Steam Reforming under Daily Start-up and Shut-Down (Dss)-Like Operation over CuFe₂O₄ Spinel and Alumina Composite Catalysts," *Appl. Catal., A*, **409-410** [1-2] 91-8 (2011).
 79. C. Diagne, H. Idriss, and A. Kiennemann, "Hydrogen production by ethanol reforming over Rh/CeO₂-ZrO₂ catalysts," *Catal. Commun.*, **3** [1] 565-571 (2002)
 80. H.-S. Roh, A. Platon, Y. Wang, and D.L. King, "Catalyst Deactivation and Regeneration in Low Temperature Ethanol Steam Reforming with Rh/CeO₂-ZrO₂ Catalysts," *Catal. Lett.*, **110** [1-2] 1-6 (2006).
 81. A. Simson, R. Farrauto, and M. Castaldi, "Steam Reforming of Ethanol/Gasoline Mixtures: Deactivation, Regeneration and Stable Performance," *Appl. Catal., B*, **106** [3-4] 295-303 (2011).
 82. Y. Zhan, D. Li, K. Nishida, T. Shishido, Y. Oumi, T. Sano, and K. Takehira, "Preparation of "Intelligent" Pt/Ni/Mg(Al)O Catalysts Starting from Commercial Mg-Al Ldhs for Daily Start-up and Shut-Down Steam Reforming of Methane," *Appl. Clay Sci.*, **45** .147-54 [3] (2009).
 83. H. Tanaka, I. Tan, M. Uenishi, M. Taniguchi, M. Kimura, Y. Nishihata, and J.i. Mizuki, "LaFePdO₃ Perovskite Automotive Catalyst Having a Self-Regenerative Function," *J. Alloys Compd.*, **408-412**, 1071-7 (2006).
 84. H. Tanaka, M. Uenishi, J. Mizuki, Y. Nishihata, and M. Kimura, "A Self-Regenerative Catalyst for Automotive Emissions Control," *Materia*, **42** [1] 571-7 (2003).
 85. J.-H. Wang and M. Liu, "Surface Regeneration of Sulfur-Poisoned Ni Surfaces under Sofc Operation Conditions Predicted by First-Principles-Based Thermodynamic Calculations," *J. Power Sources*, **176** [1] 23-30 (2008).
 86. S. Zha, Z. Cheng, and M. Liu, "Sulfur Poisoning and Regeneration of Ni-Based Anodes in Solid Oxide Fuel Cells," *J. Electrochem. Soc.*, **154** [2] B201-B6 (2007).

87. H. Tanaka and Y. Nishihata, "Self-Regenerative Function of the Intelligent Automotive Catalyst," *Kino Zairyo*, **27**, 61-70 (2007).
88. H. Tanaka, M. Taniguchi, M. Uenishi, N. Kajita, I. Tan, Y. Nishihata, J.i. Mizuki, K. Narita, M. Kimura, and K. Kaneko, "Self-Regenerating Rh- and Pt-Based Perovskite Catalysts for Automotive-Emissions Control," *Angew. Chem., Int. Ed.*, **45**, 5998-6002 (2006).
89. H. Tanaka, M. Uenishi, M. Taniguchi, I. Tan, K. Narita, M. Kimura, K. Kaneko, Y. Nishihata, and J.i. Mizuki, "The Intelligent Catalyst Having the Self-Regenerative Function of Pd, Rh and Pt for Automotive Emissions Control," *Catal. Today*, **117** [1] 321-8 (2006).
90. M. Uenishi, M. Taniguchi, H. Tanaka, M. Kimura, Y. Nishihata, J. Mizuki, and T. Kobayashi, "Redox Behavior of Palladium at Start-up in the Perovskite-Type LaFePdO_x Automotive Catalysts Showing a Self-Regenerative Function," *Appl. Catal., B*, **57** [1] 267-73 (2005).
91. N. Abatzoglou, C. Fauteux-Lefebvre, J. Blanchard, and F. Gitzhofer, Universite de Sherbrooke, Can. . "Steam Reforming of Hydrocarbonaceous Fuels over a Ni-Alumina Spinel Catalyst," Pat. WO2011020194A1, 2011.
92. B.C. Enger, R. Lodeng, and A. Holmen, "Ni and Ni-Co Spinel Catalysts in the Partial Oxidation and Steam Reforming of Methane," *Prepr. - Am. Chem. Soc., Div. Pet. Chem.*, **53** [1] 80-1 (2008).
93. N. Salhi, A. Boulahouache, C. Petit, A. Kiennemann, and C. Rabia, "Steam Reforming of Methane to Syngas over NiAl₂O₄ Spinel Catalysts," *Int. J. Hydrogen Energy*, **36** [17] 11433-9 (2011).
94. C. Fauteux-Lefebvre, N. Abatzoglou, J. Blanchard, and F. Gitzhofer, "Steam Reforming of Liquid Hydrocarbons over a Nickel-Alumina Spinel Catalyst," *J. Power Sources*, **195** [10] 3275-83 (2010).
95. E. Nikolla, J. Schwank, S. Linic, "Direct Electrochemical Oxidation of Hydrocarbon Fuels on SOFCs: Improved Carbon Tolerance of Ni Alloy Anodes", *J. Electrochem. Soc.*, 156 [1] B1312 (2009)
96. V.R. Choudhary, K.C. Mondal, and T.V. Choudhary, "Partial Oxidation of Methane to Syngas with or without Simultaneous Steam or CO₂ Reforming over a High-Temperature Stable-NiCoMgCeO_x Supported on Zirconia-Hafnia Catalyst," *Appl. Catal., A*, **306** [1] 45-50 (2006).
97. G. Busca, U. Costantino, T. Montanari, G. Ramis, C. Resini, and M. Sisani, "Nickel Versus Cobalt Catalysts for Hydrogen Production by Ethanol Steam Reforming: Ni-Co-

- Zn-Al Catalysts from Hydrotalcite-Like Precursors," *Int. J. Hydrogen Energy*, **35** [11] 5356-66 (2010).
98. D. Harshini, Y. Kwon, J. Han, S.P. Yoon, S.W. Nam, and T.H. Lim, "Suppression of Carbon Formation in Steam Reforming of Methane by Addition of Co into Ni/ZrO₂ Catalysts," *Korean J. Chem. Eng.*, **27** [2] 480-6 (2010).
 99. S.T. Misture, "Large-Volume Atmosphere-Controlled Diffraction Furnace," *Meas. Sci. Tech.*, **14** [7] 1091-8 (2003).
 100. B. Hill, "Characterizing the Reduction of Ni_xMg_{1-x}Al₂O₄"; Ph.D Thesis. Alfred University, Alfred, NY, 2012.
 101. A.W. Budiman, S.H. Song, T.S. Chang, C.-H. Shin, and M.J. Choi, "Dry Reforming of Methane over Cobalt Catalysts: A Literature Review of Catalyst Development," *Catal. Surv. Asia*, **16** [4] 183-97 (2012).
 102. F.F. de Sousa, H.S.A. de Sousa, A.C. Oliveira, M.C.C. Junior, A.P. Ayala, E.B. Barros, B.C. Viana, J.M. Filho, and A.C. Oliveira, "Nanostructured Ni-Containing Spinel Oxides for the Dry Reforming of Methane: Effect of the Presence of Cobalt and Nickel on the Deactivation Behavior of Catalysts," *Int. J. Hydrogen Energy*, **37** [4] 3201-12 (2012).
 103. C.V.M. Gonzalez-Dela, J.P. Holgado, R. Pereniguez, and A. Caballero, "Morphology Changes Induced by Strong Metal-Support Interaction on a Ni-Ceria Catalytic System," *J. Catal.*, **257** [2] 307-14 (2008).
 104. X. Du, D. Zhang, L. Shi, R. Gao, and J. Zhang, "Morphology Dependence of Catalytic Properties of Ni/CeO₂ Nanostructures for Carbon Dioxide Reforming of Methane," *J. Phys. Chem. C*, **116** [18] 10009-16 (2012).
 105. R. Lopez-Fonseca, C. Jimenez-Gonzalez, B. de Rivas, and J.I. Gutierrez-Ortiz, "Partial Oxidation of Methane to Syngas on Bulk NiAl₂O₄ Catalyst. Comparison with Alumina Supported Nickel, Platinum and Rhodium Catalysts," *Appl. Catal., A*, **437-438** [1] 53-62 (2012).
 106. M. Ohtake, T. Yanagawa, J. Higuchi, and M. Futamoto, "Structure Analysis of Ni Thin Films Epitaxially Grown on BCC Metal Underlayers Formed on MgO₍₁₀₀₎ Substrates," *EPJ Web of Conferences*, **40**, 08004 (2013).
 107. C.I.G. Osojnik, P. Djinovic, B. Erjavec, and A. Pintar, "Effect of Synthesis Parameters on Morphology and Activity of Bimetallic Catalysts in CO₂-CH₄ Reforming," *Chem. Eng. J. (Amsterdam, Neth.)*, **207-208** [1] 299-307 (2012).

105. S.M. Bukhari and J.B. Giorgi, "Chemically Stable and Coke Resistant $\text{Sm}_{1-x}\text{Ce}_x\text{FeO}_{3-\delta}$ Perovskites for Low Temperature Solid Oxide Fuel Cell Anode Applications," *J. Power Sources*, **198** [1] 51-8 (2012).
106. M.E. Miller and S.T. Mixture, "Stoichiometric (Ni,Mg)-Cordierite Glass-Ceramics," *J. Am. Ceram. Soc.*, **93** [4] 1018-25 (2010).
107. X.-F. Ye, S.R. Wang, J. Zhou, F.R. Zeng, H.W. Nie, and T.L. Wen, "Application of a Cu-CeO₂/Ni-Yttria-Stabilized Zirconia Multi-Layer Anode for Anode-Supported Solid Oxide Fuel Cells Operating on H₂-CO Syngas Fuels," *J. Power Sources*, **196** [13] 5499-502 (2011).
108. M.A. Buccheri and J.M. Hill, "Gas Product Analysis During the Electrochemical Conversion of Dry Methane with a La_{0.3}Sr_{0.7}TiO₃ and Ni/YSZ Bi-Layer SOFC Anode," *ECS Trans.*, **35** [1] 1551-61 (2011).
109. S.A. Venancio and P.E.V. de Miranda, "Solid Oxide Fuel Cell Anode for the Direct Utilization of Ethanol as a Fuel," *Scr. Mater.*, **65** [12] 1065-8 (2011).
110. D.M. Bierschenk, E. Potter-Nelson, C. Hoel, Y. Liao, L. Marks, K.R. Poeppelmeier, and S.A. Barnett, "Pd-Substituted (La,Sr)CrO_{3-δ}-Ce_{0.9}Gd_{0.1}O_{2-δ} Solid Oxide Fuel Cell Anodes Exhibiting Regenerative Behavior," *J. Power Sources*, **196** [6] 3089-94 (2011).
111. B.E. Hill and S.T. Mixture, "Atomic Scale Mechanisms in the Reduction of Nickel-Magnesium Aluminate Spinel," *J. Am. Ceram. Soc.*, **96** [11]3603-08 (2013).
112. Office of Energy Efficiency & Renewable Energy, "Types of Fuel Cells" (2014) Accessed on: November 2014. Available at <<http://energy.gov/eere/fuelcells/types-fuel-cells>>
113. E.J.W. Verwey and E.L. Heilmann, "Physical properties and cation arrangement of oxides with spinel structures," *J. Chem. Phys.* **15** [4] 174-180 (1947).